



HAL
open science

A new robust discharge estimation method applied in the context of SWOT satellite data processing

Igor Gejadze, Pierre-Olivier Malaterre, Hind Oubanas, Victor Shutyaev

► To cite this version:

Igor Gejadze, Pierre-Olivier Malaterre, Hind Oubanas, Victor Shutyaev. A new robust discharge estimation method applied in the context of SWOT satellite data processing. *Journal of Hydrology*, 2022, 610, pp.127909. 10.1016/j.jhydrol.2022.127909 . hal-03745573

HAL Id: hal-03745573

<https://hal.inrae.fr/hal-03745573>

Submitted on 22 Jul 2024

HAL is a multi-disciplinary open access archive for the deposit and dissemination of scientific research documents, whether they are published or not. The documents may come from teaching and research institutions in France or abroad, or from public or private research centers.

L'archive ouverte pluridisciplinaire **HAL**, est destinée au dépôt et à la diffusion de documents scientifiques de niveau recherche, publiés ou non, émanant des établissements d'enseignement et de recherche français ou étrangers, des laboratoires publics ou privés.



Distributed under a Creative Commons Attribution - NonCommercial 4.0 International License



Research papers

A new robust discharge estimation method applied in the context of SWOT satellite data processing

I. Gejadze^{a,*}, P.-O. Malaterre^a, H. Oubanas^a, V. Shutyaev^b^a G-EAU, Univ. Montpellier, AgroParisTech, BRGM, CIRAD, IRD, INRAE, Institut Agro, INRAE, 361 Rue J.F. Breton, BP 5095, 34196, Montpellier, France^b Marchuk Institute of Numerical Mathematics, Russian Academy of Sciences (RAS), Moscow Institute of Physics and Technology, 119333 Gubkina 8, Moscow, Russia

ARTICLE INFO

This manuscript was handled by Emmanouil Anagnostou, Editor-in-Chief

Keywords:

SWOT satellite mission
Discharge estimation
Ill-posedness
Bias
Bayesian estimation
Variational data assimilation
Saint-Venant hydraulic model
SIC² software

ABSTRACT

Knowing river discharge is vital for monitoring the fresh water cycle at the global scale. The Surface Water and Ocean Topography (SWOT) satellite mission will map river water surface elevations and inundated areas for rivers wider than one hundred meters worldwide. These observations can be used for estimating the river discharge. It is the global coverage which makes these observations particularly valuable, however in many cases there will be no data on the bathymetry and river bed properties available. That is why the problem of discharge estimation using solely the SWOT-type observations has received a noticeable attention recently.

The attempts to solve this problem have expectedly confirmed that it is highly ill-posed and, therefore, additional data is useful. In particular, the use of the mean discharge estimates retrieved from the global scale hydrological databases (e.g. the Global Water Balance Model) have been accepted. However, taking into account the accuracy of such estimates and the issue of their relevance to the current time period, the problem is still posing a serious challenge. For example, in the results obtained by different methods reported up to date, the estimated hydrograph may suffer from a significant bias, which often makes a major contribution to the total estimation error.

In this paper a new estimation method is suggested, which is specially designed to reduce the solution bias. The concept of this method is similar to the one of the Variational Expectation–Maximization method, however its perception and implementation are original and problem-oriented. In our method, the mean values of the unknown variables are obtained using the Bayesian estimator, whereas the ‘shape’ functions are updated using the variational data assimilation or generated directly using the inverted simplified hydraulic model. The two steps constitute an estimation cycle, which can be repeated after information exchange.

The method has been validated using two available testing sets including 51 cases in total. It has demonstrated a much better robustness and reliability than the variational data assimilation method, and quite a promising performance in terms of accuracy. Since the proof of the concept was in the focus of this study, the issue of computational feasibility was not a priority. Nevertheless, the method in its current form can be applied at local/regional or basin scales. For a possible global scale application, a generalized discharge estimator is suggested, where the major computational burden falls on the ‘learning’ stage, which is separated from the discharge prediction algorithm.

1. Introduction

River discharge is a key piece of information for efficient allocation of water resources, assessment of flood hazards and management of human water-related activities (Oki and Kanae, 2006). Despite its importance, the publicly available database of in situ river discharge is steadily declining over the past decades due to decreasing numbers of

gauge stations (financial and security reasons), data sharing issues for trans-boundary rivers (Biancamaria et al., 2011) and irregular distribution of the ground network (Biancamaria et al., 2016). In fact, the number of available runoff gauging stations has decreased by about 75% during the period 1970–2015 (Tourian et al., 2017). A number of important basins, mainly in developing countries in Africa, Asia and South America no longer have any operational gauge stations and real-

* Corresponding author.

E-mail addresses: igor.gejadze@inrae.fr (I. Gejadze), pierre-olivier.malaterre@inrae.fr (P.-O. Malaterre), hind.oubanas@inrae.fr (H. Oubanas), victor.shutyaev@mail.ru (V. Shutyaev).

<https://doi.org/10.1016/j.jhydrol.2022.127909>

Received 11 August 2021; Received in revised form 28 April 2022; Accepted 1 May 2022

Available online 8 May 2022

0022-1694/© 2022 Elsevier B.V. All rights reserved.

time access to in situ discharge is mostly available only in developed countries (Tourian et al., 2017; Revel et al., 2021). The loss of these primary observations impairs our ability to represent and manage river systems.

Remote sensing has been recently gaining attention as a valuable tool for the hydraulic/hydrology community attempting to complement the ground networks by filling the temporal and spatial gaps (McCabe, 2017). Although inland water observation from space is a challenging research topic due to the complexity of river systems and lakes, recent advances in satellite observation technology are expected to enhance our knowledge of fresh water resources on the global scale (Marcus and Fonstad, 2010). In this respect, the Surface Water and Ocean Topography (SWOT) satellite, due to launch in late 2022 (Durand, 2010), is the first mission dedicated to hydraulics/hydrology and mesoscale oceanography. It will provide two-dimensional observations of water surface elevation (WSE), width, and slope, simultaneously, across its 120-km-wide swath using a Ka-band Radar Interferometer (KaRIN) (Biancamaria et al., 2016). The fine spatial resolution of SWOT will enable observing rivers wider than 50–100 m with unprecedented accuracy, generally over 5–10 days intervals depending on the latitude and longitude of the river, during a 21 days repeat-cycle orbit (Biancamaria et al., 2016).

Since river discharge is not directly observable, recent studies have demonstrated potential approaches for estimating the SWOT discharge product from its direct observations. Several complementary approaches were designed for gauged and ungauged basins within the SWOT Discharge Algorithm Working Group (SWOT DAWG). The proposed algorithms offer increasing levels of complexity in terms of representation of the river dynamics and the involved optimization techniques. Among them, the so-called Mass conserved Flow Law Inversion (McFLI) algorithms (Durand et al., 2014; Garambois and Monnier, 2015; Gleason and Durand, 2020; Hagemann and Gleason, 2017) rely on the assumption of mass conservation between a set of consecutive reaches to estimate channel friction parameters and a reference cross-sectional area of flow (Frasson et al., 2021). Five such algorithms AMHG (Gleason et al., 2014), GaMo (Garambois and Monnier, 2015), MetroMan (Durand et al., 2014), MFG and MFCR (Durand et al., 2016) have been validated on the testing set including 19 rivers with different hydraulic properties (called PEPSI-1), with the discharge estimation accuracy about 35% relative root-mean-square error (RRMSE) (Durand et al., 2016).

The McFLI approaches have shown a promising performance, however, their implementation and evaluation have revealed some issues that could hinder their accuracy and applicability (Andreadis et al., 2020). In this respect, algorithms based on hydraulic models and data assimilation (DA) approaches have been developed to better account for the river dynamics with respect to the SWOT spatial and temporal coverage. These include the Variational Data Assimilation using the SIC² hydraulic model (SIC4DVAR) (Gejadze and Malaterre, 2017; Oubanas et al., 2018; Oubanas et al., 2018), the Hierarchical Variational Discharge Inference (HiVDI) (Larnier et al., 2020) and the SWOT Assimilated Discharge (SAD) (Andreadis et al., 2007; Andreadis et al., 2020). While SIC4DVAR and HiVDI algorithms assimilate SWOT observations into one-dimensional unsteady-state Saint-Venant models, SIC² (Simulation and Integration of Control for Canals, (<https://sic.g-eau.fr/?lang=en>) and DASSFLOW Saint-Venant, respectively, using variational DA methods, SAD algorithm combines the Ensemble Kalman Filter (EnKF) (Evensen, 1994) and gradually varying steady-state flow equations to estimate discharge.

Another validation step was later performed on the testing set including 32 rivers (called PEPSI-2), involving some of the above-mentioned McFLI and DA algorithms to assess the accuracy of the expected SWOT discharge product (Frasson et al., 2021). This study has explored the factors that control the performance of the discharge estimation algorithms. The results demonstrated that the most influential ones are the quality of a priori mean discharge, the accuracy of the flow law and the hydraulic variability over the observed period (Frasson

et al., 2021).

As the SWOT satellite has not yet been launched, the potential benefits of assimilating future SWOT observations into hydrodynamic models have been assessed in Oubanas et al. (2018) and Oubanas et al. (2020) using observing system simulation experiments (OSSEs). Synthetic SWOT observations were generated using SWOT High Resolution simulators to emulate the expected performance of the KaRIN instrument (Frasson et al., 2017; Domeneghetti et al., 2018). Different discharge algorithms were evaluated in this framework on several river basins. In this respect, SIC4DVAR was tested on the Garonne river (Oubanas et al., 2018) as well as the Po and Sacramento rivers (Oubanas et al., 2018) to estimate river discharge, bathymetry and friction simultaneously. Other studies have attempted multi-satellite assimilation to estimate river discharge, by combining either different altimetry data (Tourian et al., 2017; Domeneghetti et al., 2021) or altimetry together with SWOT simulations (Oubanas et al., 2020).

Further experience with SIC4DVAR being applied on the complete set of PEPSI cases has revealed some drawbacks of this method. That is, the problem of simultaneous estimation of discharge, bathymetry and friction coefficients is ill-posed in the sense of the 2nd Hadamard's condition (uniqueness). In practical applications, this issue is also known as 'equifinality'. This implies that the same model outputs at a given numerical precision can be produced with multiple (potentially infinite) combinations of unknown variables, which require some regularization to be applied. However, simply penalizing the distance between the estimate and its prior (which would be a standard regularization technique) may not be very useful with this type of ill-posedness. That is, the estimate could be totally impacted by the choice of the prior/background and background error covariance matrix. This is exactly what has been encountered in numerical tests involving SIC4DVAR. Moreover, the validity of the Gaussian assumption, which is the basis of variational DA, has appeared to be highly questionable. The mentioned issues are quite common in a variety of applications.

In order to deal with estimation problems of that type we develop a new robust estimation method. The method implements the idea of a separate treatment of the mean values of the time- or space-dependent variables and the corresponding shape functions. The mean values are estimated as expectations (probabilistic means) of the corresponding low-dimensional posterior distribution (generally non-Gaussian) using the direct Bayesian approach, whereas the shape functions are estimated using the variational DA approach, subjected to some additional constraints. Thus, the robustness is achieved because the conditional expectation is almost certainly unique (unlike modes). The two estimation steps are combined within a cycle, which can be repeated after information exchange. Overall, the procedure represents a multilevel algorithm, where different elements of the solution are subjected to different treatment at different levels. In this paper we present an adapted version of the method, i.e. the one which has been applied to the discharge estimation problem in the SWOT data assimilation context. It shall be called the SIC-BVC method, where BVC stands for the Bayesian Variational Cyclic algorithm. A rigorous consideration of the BVC method in its general form will be reported in a specialized review (computational mathematics, computer science). Let us note that SIC-BVC is using the SIC model, but also the Integrated Modified Gauckler-Manning-Strickler (GMS) model, which has been developed in this study.

The idea behind our method is similar to the Variational Maximum Likelihood method (Beal, 2003; Beal et al., 2003; McLachlan and Krishnan, 2007), also referred to as Variational Expectation-Maximization method. This is, essentially, a semi-Bayesian estimation approach, where for a subset of model parameters a Bayesian posterior distribution is constructed, while for the remaining parameters the maximum likelihood point estimates are evaluated. However, the implementation of this basic idea in our method is original. Let us note that it should not be confused with the Variational Bayesian method

(Blei et al., 2017).

The averaged accuracy of the discharge estimates obtained by our method has been assessed using different performance metrics. It seems to be superior in comparison to the accuracy of results obtained by other methods on the same testing set and reported up to date. However, the method is computationally complex, expensive, and its running may presently require human supervision. Thus, the complete setting cannot be run ‘blindly’, in close-to-real time and at the global (world) scale. In order to make these options available we suggest a generalized discharge estimator based on the Integrated Modified Low-Froude GMS model mentioned above. This estimator includes the likelihood matrix, which incorporates all the complexity of the method. Running the estimator with the **best currently available** likelihood matrix requires very little computational resource. The updated likelihood can be obtained by processing the SWOT data in a re-analysis mode, then supplied to the user.

The paper is organized as follows. Section 2 describes the pre-processing stage, where a part of the river bathymetry is defined from geometrical considerations, given a set of the elevation-width pairs observed at different (arbitrarily distributed) spatial locations and time instants. This part of the bathymetry is referred as ‘dry’. Section 3 describes the hydraulic models involved in SIC-BVC method. Section 4 describes the new discharge estimation method SIC-BVC, which is an adapted version of the BVC method, and, also, the generalized discharge estimator for the possible real-time global scale use. In Section 6 the results of using the SIC-BVC method on the complete PEPSI testing set are presented. The main findings are summarized in Conclusions.

2. Pre-processing SWOT observations

In this Section we discuss the method for estimating the bathymetry using solely the SWOT data. First of all, we distinguish ‘dry’ and ‘wet’ parts of the bathymetry. At a given spatial location, the ‘dry’ bathymetry describes the river bed above the lowest water level measured by the satellite at least once over the total observation period. This part is estimated from the SWOT data using a data-driven approach, which involves different steps: outlier removal, sorting, smoothing, piece-wise linear interpolation with reduced number of points and under some constraints. The ‘wet’ bathymetry part is considered to be a rectangular channel of an unknown variable depth below the dry part. The width of this channel is equal to the width of the dry bathymetry at its lowest point (interface between the two parts).

Since the 1.5D Saint–Venant hydrodynamic model (SIC²) is used for hydraulic simulations (Baume et al., 2005; Malaterre et al., 2014), the bathymetry has to be defined by a set of cross-sections described, for example, in the bed width-elevation format $w(x_i, z), i = 1, \dots, I_s$, located along a center line at the corresponding longitudinal abscissas x_i . Unlike 1D models, the 1.5D models allow several connected channels (anabranching or braided rivers), several beds (minor, medium, major or storage) inside a channel and in-line or lateral reservoirs to be introduced. In the SWOT context, the braided rivers have been studied in Pujol et al. (2020) and Rodriguez et al. (2021), where the authors check for a need of any special treatment (in comparison to a single channel river), and the validity of the Modified GMS equation in terms of its use for the operational discharge product. Presently, in the SWOT RiverObs software and the SWORD database (Altenau et al., 2021), the braided rivers are represented by a single channel aggregating all sub-channels.

Thus, the SWOT observations provided after treatment of the pixel cloud by RiverObs are of the same type as for a single channel: a set of pairs $\{h^*(x, t), w^*(x, t)\}$, where h^* is an observed water surface elevation h and w^* is an observed water surface top width W at different locations x_i and time instants t_j . In addition, the discharges from the global Water Balance Model (Wisser et al., 2010) are provided, representing the mean values over the period 1961–2010 at the more or less relevant spatial locations. These discharges (we denote them as Q_{WBM}) are available at

the reach level from the SWORD database (Altenau et al., 2021). Since they are coming from uncalibrated models, they can be used for the so-called ‘unconstrained SWOT discharge product’, which is the framework of our study. Let us note that other discharge estimates are also available in the SWORD database, such as GRADES (Lin et al., 2019; Yuan Yang et al., 2021). These estimates, however, can only be used in the so-called ‘constrained SWOT discharge product’, since they have been produced using the calibrated models involving in situ gauging data.

In terms of different beds inside a single channel, separated either by the elevation or width limits, we note that many natural rivers often have several such beds with different friction and hydraulic properties. One can distinguish the ‘minor’ bed, the ‘medium’ bed having more friction (for example, due to the presence of vegetation and debris, instead of clean clay and rock) and, sometimes, a ‘major’ or ‘storage’ one. In this paper we only consider two beds: the minor and the medium, having two different friction coefficients. The mass and momentum exchange between these beds are modeled using the Debord formula as explained in Section 3.1. Delimitation of the minor and medium beds can be defined based on different grounds, such as those in the slope-break method (Schaperow et al., 2019; Mercel et al., 2013), for example. In this paper, the interface between the minor and medium beds coincides with the interface between the dry and wet parts of the bathymetry. This simplifying hypothesis helps to formulate a better conditioned estimation problem.

2.1. Dry bathymetry

As mentioned above, SIC² needs the bathymetry represented by the cross-sections described in the width-elevation format. This implies that cross-sections are symmetrical, which is a classical simplification used in 1D or 1.5D hydraulic modeling. Conveniently, the SWOT observations will be provided to the users exactly in this format. Thus, the simplest option would be to define the dry bathymetry directly from the raw SWOT data. However, realistic SWOT observations will contain errors of very different nature. This will result into the following issues.

First, the observed width $w^*(x, h^*)$ could be an irregular function of h^* due to errors in the SWOT data. In this case the directly derived cross-section shape would be unusual for natural rivers, which generally must be a monotonic increasing function. In terms of hydraulic behavior, the oscillating cross-section shape will result into an over-estimated wetted perimeter and, therefore, unrealistic values of friction. Besides, in addition to the regular (inherent) SWOT noise, there could be outliers, which must be removed. The second issue is that the RAM and CPU requirements for the Saint–Venant solver could be quite heavy, unless we use approximated cross-sections, i.e. those defined by a small number of the width-elevation points, sufficient to replicate the shape. The mentioned reasons justify the pre-processing of the raw SWOT observations (as provided in the SWORD database) to generate a useful bathymetry approximation. Since this processing algorithm could potentially be applied at the global scale to millions of cross-sections (nodes) of the SWORD database, the low computational cost and robustness of this algorithm have been the essential design constraints.

The algorithm is a loop over the cross-sections. For each cross-section i located at x_i the associated data subset $\{h^*(x_i, t_j), w^*(x_i, t_j)\}$ (i -subset) is processed using the following steps.

1. Removing outliers using a sliding time window (5 time-step length) and the 3-sigma test on the time series of w^* .
2. Sorting the i -subset by increasing values of the water elevation h^* . The ordered i -subsets are presented in Fig. 1. Here the upper plot shows the observed elevations h^* as a function of index in green, and the mid plot – the observed half-width $w^*/2$ as a function of index in red. One can notice that the observed width shows strong oscillations. The magnitude of oscillations is significantly large in the

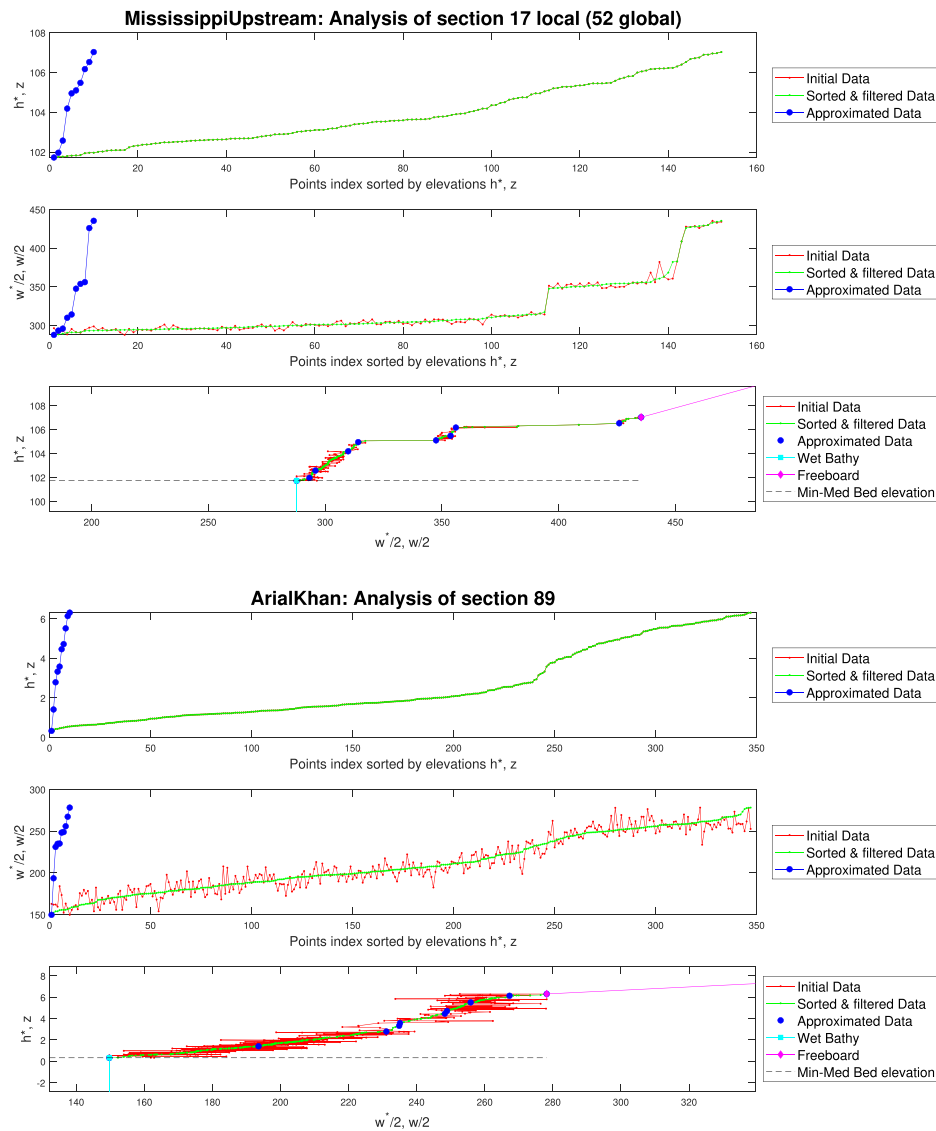


Fig. 1. Bathymetry at cross-section 17 of the Mississippi river (PEPSI-1), and at cross-section 89 of the Arial Khan river (PEPSI-2).

ArialKhan case, PEPSI-2, where the ‘full uncertainty’ case is considered (Frasson et al., 2021).

3. Re-arranging the series of w_i^* in such a way that it also becomes a monotonically increasing function of the index. This is again done by sorting: the smallest width w^* is attributed to the smallest h^* , the next smallest width w^* is attributed to the next smallest h^* , end so on. The result of this procedure (i.e. re-ordered w^*) can be seen in the mid plot in green. Finally, the bottom plot in Fig. 1 shows the shape of the section (parametric curve constructed from the elevation and width series) in red for the raw data, and in green for the sorted-filtered data. One can consider the sorted-filtered cross-section shape in green as a desired approximation of the raw data based shape in red. The presented double sorting procedure has the advantage of being very fast and robust, while naturally imposing the monotonic increase condition on the function $w^*(x, h^*)$, $\forall x$. Some other classical smoothing and data filtering procedures available in Matlab (e.g. *polyfit*, *roess*) have been tested, but did not show any significant advantages in comparison to this simple approach.

4. Approximating the sorted-filtered cross-section shape (green line in the bottom plot) by a piece-wise linear function using a limited number of points $\{w_n, z_n\}$, $n = 1, \dots, N_p$. This problem is not trivial, since neither the number of points N_p , not their locations on the

parametric curve are known in advance. An iterative procedure has been developed where some intermediate points are added to minimize the distance between the original shape and its piece-wise linear approximation. The procedure stops when a minimum distance is obtained for all points (e.g. 15 cm), or when the allowed number of points is reached (e.g. 10 points). For all PEPSI test cases we observed that from 5 to 10 points have been sufficient to approximate the original shape with less than 15 cm distance error. In both cases presented (Mississippi US and ArialKhan) 10 points are necessary. The resulting optimized points are presented in the upper plot (z series), mid plot (w series) and in the parametric form $w(z)$ in blue line with circles. Then, the additional 2 points of this approximation are extrapolated to provide a freeboard (part of the cross-section above the largest observed water level). These are shown at the bottom plot in magenta line with circles.

The procedure being applied to all sections at different locations gives an estimation of the dry bathymetry along the channel under consideration, as presented in Fig. 1. In the Pepsi 1/2 tests the river case includes a sequence of contiguous reaches, where the ‘good’ and ‘bad’ ones are distinguished. The ‘bad’ reaches are usually those with an obstruction (dam, drop, weir, lock) and/or with a strong tidal influence.

To the best of our knowledge, the algorithms presented in Durand et al. (2016) and Frasson et al. (2021) consider only ‘good’ reaches. Moreover, the discharge is computed for each one separately, then the results are averaged. In contrast, for a given river case we reveal the longest sequence of contiguous ‘good’ reaches, which defines the stretch of the river to be considered in the modeling and estimation process.

The presented algorithm can be run at different spatial scales without any further modification, from one to a series of reaches. A low cost version this algorithm is also implemented in the Confluence platform at the 1-Reach level. Several alternatives are possible and will also be tested in the future. The selection of reaches as well as other treatments described in this section are done fully automatically.

2.2. Wet bathymetry

Defining the wet bathymetry (unobserved part of the river bed) is a very different task. This problem has been investigated by many authors either based on geomorphology or hydraulic geometry methods (Leopold and Maddock, 1953; Gleason et al., 2014; Neal et al., 2021), or hydraulic based methods such as Modified GMS equation methods (uniform or non-uniform), or others. A literature review is available in Neal et al. (2021) explaining the advantages and drawbacks of different methods. Some methods such as the hydraulic geometry, curve fitting or slope break methods do not split the bathymetry into the dry and wet parts, but rather take into account the zone below the bank full depth limit.

In our method, we define the wet bathymetry as a rectangular channel below the dry part, with unknown bottom elevation $z_b(x)$ and known width $w(x) = w_1(x)$, where $w_1(x)$ is the width of the first (lowest) point of the estimated dry bathymetry. The corresponding elevation $z_1(x)$, also being the elevation of the interface between the dry and wet parts, serves as a reference level, with respect to that the bottom elevation of the wet part (and of the whole cross-section) is defined as follows:

$$z_b(x) = z_1(x) + b(x) \quad (1)$$

where $b(x) < 0$ is a strictly negative update to be estimated. The wet bathymetry is shown in light-blue in Fig. 1, bottom plot, and in Fig. 2.

Let us denote $p_g^*(x)$ – the optimized set of points $\{w_n(x), z_n(x)\}$, $n = 1, \dots, N_p(x)$ describing the dry bathymetry at location x . Since the wet bathymetry is defined by $b(x)$, the whole bathymetry is denoted as $p_g(x) = (b(x), p_g^*(x))^T$. These notations will be used throughout the text. We also keep in mind that x is a discrete variable x_i , $i = 1, \dots, I_s$, however the index is dropped when possible to simplify notations.

3. Hydraulic models involved

3.1. Saint-Venant hydraulic model

The hydraulic model is defined on a set of closed-line segments or connected ‘reaches’. The spatial discretization along reach number i_r produces a set of coordinates x_{i_r, i_s} , also called longitudinal abscissas (or ‘stations’), each having the associated global index i and its own position vector $\vec{r}_i = (x'_i, y'_i, z'_i)$ in the global coordinate system (bathymetry). Given \vec{n}_i is a predominant flow direction at x_{i_r, i_s} , a hydraulic cross-section S_i is defined by a set of points on a plane $\vec{n}_i \cdot (\vec{r} - \vec{r}_i) = 0$, describing the bed profile. For each cross-section this data allows us to compute for any given water level h : the wetted area function $A(h, p_g)$, the wetted perimeter function $P(h, p_g)$, the hydraulic radius function $R(h, p_g)$ and the top width function $W(h, p_g)$, where p_g are geometric parameters of the corresponding cross-section. For a given reach, p_g is a function of the longitudinal abscissa x .

For a ‘regular’ section, the shallow water flow in the longitudinal direction x is described by the Saint-Venant equations:

$$\frac{\partial A}{\partial t} + \frac{\partial Q}{\partial x} = Q_l, \quad (2)$$

$$\frac{\partial Q}{\partial t} + \frac{\partial Q^2/A}{\partial x} + gA \frac{\partial h}{\partial x} = -gAS_f + K_l Q_l v, \quad (3)$$

$$t \in (0, T], x \in (0, L)$$

where $Q(x, t)$ is the discharge, $h(x, t)$ is the water level, $v(x, t) = Q/A$ is the mean velocity, $Q_l(x, t)$ is the lateral discharge, $K_l(x)$ is the lateral discharge coefficient and S_f is the friction slope term dependent on the Strickler coefficient $k(x)$ (inverse of the Manning coefficient):

$$S_f = \frac{Q|Q|}{k^2 A^2 R^{4/3}}. \quad (4)$$

The initial condition for Eqs. 2,3 is

$$h(x, 0) = h_0(x), Q(x, 0) = Q_0(x). \quad (5)$$

Boundary conditions are defined at the boundary nodes: the inflow discharge $\mathcal{Q}(t)$ is used for the upstream node, and the elevation $h_L(t)$ – for the downstream node. Let us underline here that **no rating curve is used** as a boundary condition in this study.

In the classical (single bed) formulation, the friction term is defined as in (4). However, in modeling natural rivers several beds with different friction coefficients are often considered. These beds usually correspond

Case MississippiUpstream river (sections 36 to 65)

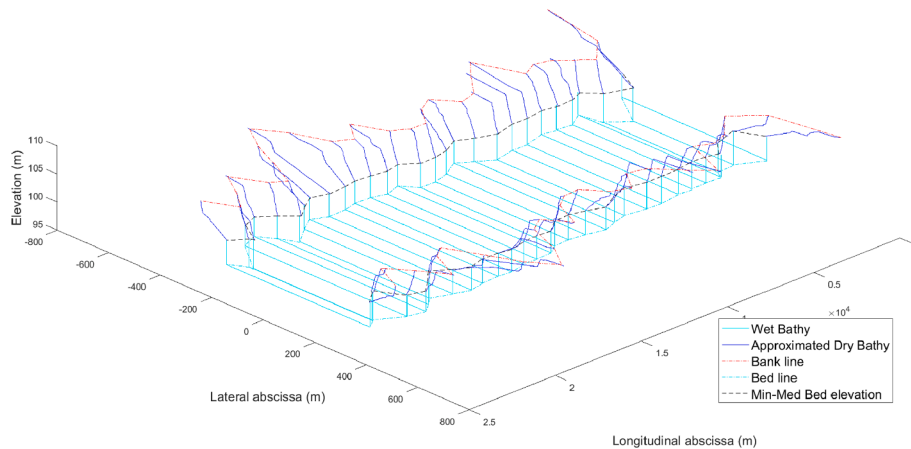


Fig. 2. Bathymetry around cross-section 17 of the Mississippi river (reach 6, PEPSI-2).

to different lateral zones of the river sections and to different depths. In the SIC hydrodynamic model, we have the minor (mn) and medium (md) beds, interacting via the mass and momentum exchange according to the Debord formulas (Nicollet and Uan, 1979), which have an empirical nature. In HEC-RAS model one can have multiple beds, described by the Einstein formulas (known as Divided Channel Method (DCM)) to combine the contribution of different beds with different Manning coefficients. The latter approach neglects any flow interactions between beds and, therefore, is less accurate.

The two-bed (or Debord) formulation is based on the following equations:

$$Q = Q_{mn} + Q_{md}, \quad (6)$$

where

$$Q_{mn} = \phi k_{mn} A_{mn} R_{mn}^{2/3} S_f^{1/2} := D_{mn} S_f^{1/2},$$

$$Q_{md} = k_{md} (A_{md}^2 + A_{mn} A_{md} (1 - \phi^2))^{1/2} R_{md}^{2/3} S_f^{1/2} := D_{md} S_f^{1/2},$$

$$\phi = \begin{cases} \phi_0, & r > 0.3 \\ 0.5(1 + \phi_0) + 0.5(1 - \phi_0) \cos(\pi r / 0.3), & r \leq 0.3 \end{cases},$$

$$\phi_0 = 0.9 \left(\frac{k_{mn}}{k_{md}} \right)^{-1/6}, \quad r = \frac{R_{md}}{R_{mn}}.$$

Here, D_{mn} and D_{md} are called the conveyance variable of the minor and the medium bed, respectively. By definition $k_{mn} > k_{md}$. We note that the friction slope S_f is supposed to be the same in both the minor and the medium beds. This is a classical assumption that is also made in the DCM method. By summing the equations for Q_{mn} and Q_{md} we obtain:

$$Q = (D_{mn} + D_{md}) S_f^{1/2}.$$

Thus, the Saint-Venant equations in the two-bed formulation remain the same while replacing the friction term (4) by:

$$S_f = \frac{Q|Q|}{(D_{mn} + D_{md})^2}. \quad (7)$$

Let us note that

$$A(x, t) := A(h(x, t), b(x), p_g^*(x)),$$

$$D(x, t) := D(h(x, t), k(x), b(x), p_g^*(x)),$$

where $b(x)$ and $p_g^*(x)$ are defined in Section 2. Thus, we denote the Saint-Venant model by an operator \mathcal{M}_{SV} which maps the input vector

$$X = \left(\mathcal{C}(t), h_L(t), Q_0(x), h_0(x), k_{mn}(x), k_{md}(x), b(x), p_g^*(x) \right)^T, \quad (8)$$

$$x \in [0, L], \quad t \in [0, T]$$

into the Saint-Venant solution $\{Q, h\}$:

$$(Q, h)^T = \mathcal{M}_{SV}(X), \quad Q := Q(x, t), \quad h := h(x, t), \quad x \in [0, L], \quad t \in [0, T]. \quad (9)$$

3.2. Modified Gauckler-Manning-Strickler models

The GMS formula for the friction slope (4) is often inverted to compute the discharge given some hydraulic parameters:

$$Q = kAR^{2/3} S_f^{1/2}. \quad (10)$$

Since the friction (energy or head) slope S_f is difficult to measure (we would have to measure the depth but also the velocity, so in this case we already would have the discharge estimation), it is often replaced either by the bed slope $-\partial z_b / \partial x$, or by the water slope $-\partial h / \partial x$. The resulting approximations to Eq. (10) should be called the modified 'Uniform Flow' and 'Low-Froude' GMS equations, respectively.

In natural rivers the Uniform Flow is rarely a good approximation, since the bed level and width are not regular, and the river water surface elevations are rather following M1 or M2 backwater curves (Cunge et al., 1980). However, the modified Low-Froude GMS equation can be considered as a good approximation when the Froude number is small (e.g. $Fr \leq 0.3$). In practice, this equation is likely applicable in a broader range of cases.

The latter is often the case for large rivers (e.g. see in Durand et al., 2016 where the Froude number ranges are provided for the Pepsi-1 test cases).

3.2.1. Modified Low-Froude GMS model, single-bed formulation

Following the previous assumption the Eq. (10) becomes:

$$Q = kAR^{2/3} \text{sign} \left(-\frac{\partial h}{\partial x} \right) \left| \frac{\partial h}{\partial x} \right|^{1/2}. \quad (11)$$

If we assume that the water slope is always negative, then the equation above reads as follows:

$$Q = kAR^{2/3} \left(-\frac{\partial h}{\partial x} \right)^{1/2}. \quad (12)$$

3.2.2. Modified Low-Froude GMS model, two-bed formulation

Following previous definitions, in the case of two-bed this formulation becomes:

$$Q = Q_{mn} + Q_{md} = (D_{mn} + D_{md}) \left(-\frac{\partial h}{\partial x} \right)^{1/2}. \quad (13)$$

Let us note that

$$D(x, t) := D(h(x, t), k_{mn}(x), k_{md}(x), b(x), p_g^*(x)).$$

Thus, we denote the Modified Low-Froude GMS two-bed model by an operator \mathcal{M}_{M2} which maps the input vector

$$X = \left(h(x, t), k_{mn}(x), k_{md}(x), b(x), p_g^*(x) \right)^T,$$

into the local (at point x) discharge Q :

$$Q = \mathcal{M}_{M2}(X), \quad Q = Q|_x(t), \quad t \in [0, T]. \quad (14)$$

3.2.3. Integrated Modified Low-Froude GMS, single bed formulation

One can see that Eq. (12) includes the local slope $\partial h(x) / \partial x$. In practice, this slope can be evaluated by taking the numerical derivative of the observed surface elevation, for example, using the forward derivative

$$\frac{h^*(x + \delta x) - h^*(x)}{\delta x}.$$

In reality, h^* may contain a significant error. This could become a critical issue when dealing with reaches having a small bed slope. Increasing δx (to get a more stable estimation of the derivative $\partial h(x) / \partial x$) is limited because the bathymetry may significantly vary over the interval $[x, x + \delta x]$. In order to resolve this issue we consider the following approach.

Let us rewrite (12) in the form

$$\frac{1}{k(x)A(x, t)R^{2/3}(x, t)} = \frac{1}{Q(x, t)} \left(-\frac{\partial h^*(x, t)}{\partial x} \right)^{1/2}.$$

We assume that a) $Q(x, t) > 0$ and b) $Q(x, t) \approx Q(t), \forall x \in [x, x + \delta x]$. First, the expression above is squared

$$\frac{1}{k^2(x)A^2(x, t)R^{4/3}(x, t)} = -\frac{1}{Q^2(x, t)} \frac{\partial h^*(x, t)}{\partial x},$$

then integrated over the interval $[x, x + \delta x]$

$$\int_x^{x+\delta x} k^{-2}(x)A^{-2}(x,t)R^{-4/3}dx = \int_x^{x+\delta x} -\frac{1}{Q^2(x,t)} \frac{\partial h^*(x,t)}{\partial x} dx.$$

Since $Q(t)$ does not depend on x , the right integral becomes

$$\frac{h^*(x,t) - h^*(x + \delta x, t)}{Q^2(t)}.$$

Next, we introduce

$$\delta h^*(t) = \max[0, h^*(x, t) - h^*(x + \delta x, t)]$$

Then, for $Q(t)$ we can finally write

$$Q(t) = \frac{(\delta h^*(t))^{1/2}}{\left(\int_x^{x+\delta x} k^{-2}(x)A^{-2}(x,t)R^{-4/3}(x,t)dx\right)^{1/2}}. \quad (15)$$

The advantage of the presented approach is that one can use δx big enough to get δh^* significantly larger than the observation error and to ensure that $h^*(x, t) > h^*(x + \delta x, t)$, $\forall t$. Obviously, the condition $Q(x, t) > 0$ may not be satisfied for estuarial zones, where the tidal effects are strong; yet, it can be satisfied for the residual flow (Dyer, 1973). Let us note, that the expression similar to (15) could be derived for the two-bed formulation (13).

Let us note that

$$A(x, t) := A(h^*(x, t), b(x), p_g^*(x)), \quad R(x, t) := R(h^*(x, t), b(x), p_g^*(x))$$

Thus, we denote the Integrated Modified Low-Froude GMS model as an operator \mathcal{M}_{MI} which maps the input vector

$$X = \left(h^*(x, t), k(x), b(x), p_g^*(x)\right)^T, \quad x \in [a, a + \delta] \in [0, L],$$

into the interval-averaged discharge Q :

$$Q_{MI}(t) = \mathcal{M}_{MI}(X, a, \delta). \quad (16)$$

4. Discharge estimation methodology

In the ‘idealized’ problem setup the observations $h^*(x_i, t_j)$ and $w^*(x_i, t_j)$ are provided at time instants $t_j = (j-1)\delta t$, where $\delta t = const$ is the ‘satellite revisiting period’, covering the total observation period $t \in [0, T]$. While the uniform temporal sampling has been a feature of the testing set (provided to all members of the DAWG), our method is designed for the general case of a non-uniform sampling.

Consider again the input vector of the Saint-Venant model (8):

$$X = \left(\mathcal{C}(t), h_L(t), Q_0(x), h_0(x), k_{mn}(x), k_{md}(x), b(x), p_g^*(x)\right)^T, \\ x \in [0, L], \quad t \in [0, T].$$

Out of the full input set, the dry bathymetry p_g^* is the component which is considered to be known (actually computed as described in Section 2.1). Taking into account the spatial and temporal scales involved, the influence of the initial conditions $Q_0(x), h_0(x)$ is considered negligible. Thus we define them as a steady-state solution for certain averaged conditions. In the ‘idealized’ case we may also consider the downstream elevation as an observable quantity, i.e. $h_L(t_j) = h^*(L, t_j)$. All other components of the input vector X must be estimated. These include $\mathcal{C}(t), b(x), k_{mn}(x)$ and $k_{md}(x)$. The presented estimation problem is ill-posed in terms of uniqueness (the 2nd condition of Hadamard). In order to solve this problem we use the idea of separate treatment of ‘means’ and ‘shapes’, described below.

4.1. Representation of unknown variables

Let us denote $\bar{u} := \overline{u(\psi)}$ the mean value of a function $u(\psi)$ over its domain $\psi \in [\psi^{lb}, \psi^{ub}]$, where superscripts ‘lb’ and ‘ub’ stand for ‘lower bound’ and ‘upper bound’, respectively. Then, we represent the

unknown functions as products

$$\mathcal{C}(t) = \bar{\mathcal{C}} \mathcal{C}_1(t), \quad b(x) = \bar{b} b_1(x) \frac{\bar{w}^*}{w^*(x)}, \quad k_{mn}(x) := k(x) = \bar{k} k_1(x), \quad (17)$$

where $\bar{\mathcal{C}}, \bar{b}$ and \bar{k} are the means (scalars), and $\mathcal{C}_1(t), b_1(x)$ and $k_1(x)$ are the ‘shape’ functions, such that

$$\frac{1}{T} \int_0^T \mathcal{C}_1(t) dt = 1, \quad \frac{1}{L} \int_0^L b_1(x) \frac{\bar{w}^*}{w^*(x)} dx = 1, \quad \frac{1}{L} \int_0^L k_1(x) dx = 1.$$

Representation (17) is possible because all considered means are sign-definite:

$$\bar{\mathcal{C}} > 0, \quad \bar{b} < 0, \quad \bar{k} > 0.$$

Moreover, we assume that the means are subjected to the box constraints:

$$\bar{\mathcal{C}}^{lb} \leq \bar{\mathcal{C}} \leq \bar{\mathcal{C}}^{ub}, \quad \bar{b}^{lb} \leq \bar{b} \leq \bar{b}^{ub}, \quad \bar{k}^{lb} \leq \bar{k} \leq \bar{k}^{ub}. \quad (18)$$

4.2. Shape functions

In the suggested algorithm the mean values of the distributed variables are estimated using the direct Bayesian approach, whereas the shape functions are estimated using the variational approach. However, for the discharge estimation problem the approximate shape function $\mathcal{C}_1(t)$ can be generated using the Integrated Modified Low-Froude GMS model, defined over the initial part of the reach $x \in [0, \delta]$, where $\delta \ll L$:

$$\mathcal{C}_1(t) \approx Q_1(t) := Q_{MI}(t) / \bar{Q}_{MI} \quad (19)$$

where

$$Q_{MI}(t) = \mathcal{M}_{MI}(X, 0, \delta), \quad (20)$$

$$X = \left(h^*(x, t), \bar{k} k_1(x), \bar{b} b_1(x), p_g^*(x)\right)^T, \quad x \in [0, \delta]. \quad (21)$$

It is easy to see that $Q_1 := Q_1(k_1, \bar{b}, b_1)$, but does not depend on \bar{k} , so any nonzero value can be used as a model input, for example $\bar{k} = 1$. The shape function for bathymetry (17) is chosen in the form $b_1(x) \bar{w}^* / w^*(x)$ in order to achieve the equal update of the wet cross-sections $A(x, t)$ along the reach, due to the change of \bar{b} (for $b_1(x) = 1$).

4.3. Cost functions and likelihood function

For estimating the means of the distributed variables we define a cost-function involving the Saint-Venant model, assuming the outflow elevation $h_L(t)$ is equal to the observed elevation at the last section $h^*(L, t)$; and the minor and medium bed friction are the same $k_{mn}(x) = k_{md}(x) = \bar{k} k_1(x)$ (in fact, any ratio between k_{mn} and k_{md} can be used, given $k_{md} < k_{mn}$ holds). Let \mathcal{N} be an observation operator which maps the Saint-Venant model output into the observation space \mathcal{Y} , whereas $Y^* \in \mathcal{Y}$ is the vector of observations. In the particular case considered, this vector directly includes the observed elevations $h^*(x, t)$, given at time instances t_i and spatial locations x_j . More generally, Y^* could be a function of the primary SWOT data. Thus, the cost function is defined as follows:

$$J_0(\bar{\mathcal{C}}, Q_1, \bar{k}, k_1, \bar{b}, b_1) = \|\mathcal{N} \mathcal{M}_{SV}(X) - Y^*\|^2, \quad (22)$$

where

$$X = \left(\bar{\mathcal{C}} Q_1(t), h_L^*(t), \bar{k} k_1(x), \bar{b} b_1(x) \bar{w}^* / w^*(x), p_g^*(x)\right)^T, \\ x \in [0, L], \quad t \in [0, T], \quad (23)$$

and $Q_1 := Q_1(k_1, \bar{b}, b_1)$ according to (19).

The posterior expectation of $\mathcal{Q}(t)$ is given by the 3D integral involving the likelihood function \mathcal{L} and the prior distribution $\rho(\cdot)$ of the means $\bar{\mathcal{C}}, \bar{b}, \bar{k}$:

$$\widehat{\mathcal{Q}}(t) = \frac{1}{\|\cdot\|} \int \int \int \bar{\mathcal{Q}} Q_1(t) \mathcal{L}[J_0(\bar{\mathcal{C}}, Q_1, \bar{k}, k_1, \bar{b}, b_1), \alpha_1] \rho(\bar{\mathcal{C}}, \bar{b}, \bar{k}) d\bar{\mathcal{C}} d\bar{b} d\bar{k}. \quad (24)$$

Since the inflow discharge (or the reach-averaged discharge) is considered as the major variable of interest, the integration quality over $\bar{\mathcal{C}}$ must be sufficiently high, which means a small integration step. Instead, one can substitute the 3D integral by a 2D integral as follows

$$\widehat{\mathcal{Q}}(t) = \frac{1}{\|\cdot\|} \int \int \bar{\mathcal{Q}}' Q_1(t) \mathcal{L}[J_0(\bar{\mathcal{C}}', Q_1, \bar{k}, k_1, \bar{b}, b_1), \alpha_1] \times \rho(\bar{\mathcal{C}}', \bar{b}, \bar{k}) d\bar{b} d\bar{k}, \quad (25)$$

where

$$\bar{\mathcal{C}}' = \underset{\bar{\mathcal{C}}}{\operatorname{argmin}} J_0(\bar{\mathcal{C}}, Q_1, \bar{k}, k_1, \bar{b}, b_1). \quad (26)$$

In practice, implementation of (25) is more accurate and less expensive than computing the integral over $\bar{\mathcal{C}}$. The likelihood function is defined as follows:

$$\mathcal{L}[J_0(\bar{\mathcal{C}}', Q_1, \bar{k}, k_1, \bar{b}, b_1), \widehat{J}_0, \alpha_1] = \exp \left[-\frac{m}{4\alpha_1} \left(\frac{J_0(\bar{\mathcal{C}}', Q_1, \bar{k}, k_1, \bar{b}, b_1)}{\widehat{J}_0} - 1 \right)^2 \right], \quad (27)$$

where

$$\widehat{J}_0 = \min_{\bar{b}, \bar{k}} J_0(\bar{\mathcal{C}}'(\bar{k}, \bar{b}), Q_1, \bar{k}, k_1, \bar{b}, b_1). \quad (28)$$

Parameter α_1 in (27) controls the likelihood decay rate and is similar (not equivalent!) to the regularization parameter in Tikhonov's formulation (Tikhonov and Arsenin, 1977). Its value is evaluated using the L-curve approach (Hansen and O'Leary, 1993) as described in Section 4.7.

For estimating the shape functions we define the standard variational DA cost-function involving the Saint-Venant model

$$J_1(X) = \|\mathcal{N}_{SV}(X) - Y^*\|^2 + \alpha \|C^{-1/2} \sigma^{-1} (X - X^*)\|^2, \quad (29)$$

where

$$X = \left(\mathcal{Q}(t), h_L(t), k_{mn}(x), k_{md}(x), b(x), p_g^*(x) \right)^T, \quad x \in [0, L], \quad t \in [0, T]. \quad (30)$$

The penalty term in (29) includes the prior/background (known) approximation of X^* and, also, the correlation matrix C and the variance σ of the background error, which are very difficult to specify in hydraulic application. This is why the formulation contains parameter α .

4.4. Finite dimensional Bayesian estimates

Let us discretize uniformly the plane $\{\bar{b}, \bar{k}\}$ with steps

$$\Delta \bar{b} = (\bar{b}^{ub} - \bar{b}^{lb})/n_1, \quad \Delta \bar{k} = (\bar{k}^{ub} - \bar{k}^{lb})/n_2,$$

and consider the integration sample points

$$\bar{b}_i = \bar{b}^{ub} - (i-1)\Delta \bar{b}, \quad \bar{k}_j = \bar{k}^{lb} + (j-1)\Delta \bar{k}, \quad i = 1, \dots, n_1, \quad j = 1, \dots, n_2.$$

Then, integral (25) can be approximated by a sum:

$$\widehat{\mathcal{Q}}(t) = \frac{1}{\|C_0\|} \sum_{i=1}^{n_1} \sum_{j=1}^{n_2} \bar{\mathcal{Q}}'_{ij} Q_{1,i}(t) \mathcal{L}[J_{0,(ij)}, \widehat{J}_0, \alpha_1] \rho(\bar{\mathcal{C}}'_{ij}, \bar{b}_i, \bar{k}_j), \quad (31)$$

where

$$\bar{\mathcal{C}}'_{ij} = \underset{\bar{\mathcal{C}}}{\operatorname{argmin}} J_0(\bar{\mathcal{C}}, Q_{1,i}, \bar{k}_j, k_1, \bar{b}_i, b_1), \quad \bar{\mathcal{C}}^{lb} \leq \bar{\mathcal{C}}'_{ij} \leq \bar{\mathcal{C}}^{ub}; \quad (32)$$

$$i = 1, \dots, n_1, \quad j = 1, \dots, n_2,$$

$Q_{1,i}(t) = Q_1(k_1, \bar{b}_i, b_1)$ (according to (19)–(21)), and $J_{0,(ij)}$ is the corresponding value of the cost function achieved in one-directional minimization (32) and, according to (28)

$$\widehat{J}_0 = \min_{ij} J_{0,(ij)}.$$

The scaling constant in (31) is

$$C_0 = \sum_{i=1}^{n_1} \sum_{j=1}^{n_2} \mathcal{L}[J_{0,(ij)}, \widehat{J}_0, \alpha_1] \rho(\bar{\mathcal{C}}'_{ij}, \bar{b}_i, \bar{k}_j). \quad (33)$$

Next, we define the prior of $\mathcal{Q}(t)$ as follows:

$$\mathcal{Q}_{pr}(t) = \frac{1}{\|C_1\|} \sum_{i=1}^{n_1} \sum_{j=1}^{n_2} Q_{MI,(ij)}(t) \rho(\bar{Q}_{MI,(ij)}, \bar{b}_i, \bar{k}_j), \quad (34)$$

where

$$C_1 = \sum_{i=1}^{n_1} \sum_{j=1}^{n_2} \rho(\bar{Q}_{MI,(ij)}, \bar{b}_i, \bar{k}_j), \quad (35)$$

Above, the Integrated Modified GMS model output Q_{MI} is defined by (20) with

$$X = \left(h^*(x, t), \bar{k}_j k_1(x), \bar{b}_i b_1(x), p_g^*(x) \right)^T, \quad x \in [0, \delta].$$

This prior estimate is used for optimal choice of regularization parameter α_1 .

Unlike $Q_1(t)$ (which depends on \bar{b}) the shape functions $b_1(x)$ and $k_1(x)$ do not depend on \bar{b} or \bar{k} , so one can compute their posterior expectations:

$$\widehat{(\bar{b}, \bar{k})}^T = \frac{1}{\|C_0\|} \sum_{i=1}^{n_1} \sum_{j=1}^{n_2} (\bar{b}, \bar{k})^T \mathcal{L}[J_{0,(ij)}, \widehat{J}_0, \alpha_1] \rho(\bar{\mathcal{C}}'_{ij}, \bar{b}_i, \bar{k}_j). \quad (36)$$

Therefore,

$$\widehat{b}(x) = \widehat{\bar{b}} b_1(x), \quad \widehat{k}(x) = \widehat{\bar{k}} k_1(x). \quad (37)$$

These estimates will be used in the variational DA step as the background values.

Finally, one can compute the variance for $\widehat{\mathcal{Q}}(t)$ by the following formula

$$\operatorname{Var}[\mathcal{Q}](t) = \frac{1}{\|C_0\|} \sum_{i=1}^{n_1} \sum_{j=1}^{n_2} \left(\bar{\mathcal{Q}}'_{ij} Q_{1,i}(t) - \widehat{\mathcal{Q}}(t) \right)^2 \times \mathcal{L}[J_{0,(ij)}, \widehat{J}_0, \alpha_1] \rho(\bar{\mathcal{C}}'_{ij}, \bar{b}_i, \bar{k}_j), \quad (38)$$

where $\widehat{\mathcal{Q}}(t)$ is given by (31). The variance is used for choosing the optimal value of regularization parameter α_1 . It can be used, of course, as a posterior uncertainty measure.

Remark: In practice, the sweep over the 2D trial plane $\{\bar{b}, \bar{k}\}$ can be interrupted before reaching the plane bounds to reduce the computational cost. It has been noticed that in many cases (e.g. for rivers having a significant bed slope) the cost function

$$\widehat{J}_{0,i} = \min_j J_{0,(ij)} \quad (39)$$

is a monotonically increasing function of index i (depth), starting from some value i^* . This implies that the likelihood which corresponds to $\widehat{J}_{0,i} > \widehat{J}_{0,i^*}$, where ϵ is a chosen constant (e.g. $\epsilon = 10$), has become too

small to noticeably contribute to the sum in (31) and, therefore, the i -loop can be stopped. Then, the lower bound for \bar{b} is subsequently redefined as

$$\bar{b}^{lb} = \bar{b}_i.$$

4.5. Specification of the prior PDF

First assumption is that the prior joint PDF is a product of marginal distributions, for example

$$\rho(\bar{\mathcal{C}}'_{ij}, \bar{b}_i, \bar{k}_j) = \rho(\bar{\mathcal{C}}'_{ij})\rho(\bar{b}_i)\rho(\bar{k}_j).$$

Since we can guess on the bounds of the means based on physical considerations and/or available data from side sources, for the prior PDF we use the β -type distribution defined over the interval $[0, 1]$ and dependent on two shape parameters. A change of variables allows a PDF with the desired mode μ and spread σ to be constructed. Thus, for any scalar variable ψ , by $\rho(\psi)$ we actually mean

$$\rho(\psi) := \rho\left(\frac{\psi - \psi^{lb}}{\psi^{ub} - \psi^{lb}}, \mu_\psi, \sigma_\psi\right), \psi \in [0, 1], \mu_\psi \in [0, 1], \sigma_\psi > 0. \quad (40)$$

Let us note that $\rho(\psi)$ approaches the uniform distribution with $\sigma \rightarrow \infty$, for any μ . In particular, for $\bar{\mathcal{C}}$ we use

$$\mu_Q = \frac{Q_{WBM} - \bar{Q}^{lb}}{Q^{ub} - \bar{Q}^{lb}}, \quad (41)$$

where

$$\bar{Q}^{lb} = Q_{WBM}/5, \quad \bar{Q}^{ub} = 5Q_{WBM}. \quad (42)$$

This results into a highly skewed PDF presented in Fig. 3. In the special case of computing the bounds for the posterior $\hat{\mathcal{C}}(t)$ in (31) we use $\mu_Q = \epsilon$ (for the lower bound) and $\mu_Q = 1 - \epsilon$ (for the upper bound), with a small enough σ_Q . Concerning \bar{b} and \bar{k} , the parameters are chosen such that the resulting PDFs are close to the uniform distribution, see again in Fig. 3.

4.6. Variational estimation

4.6.1. Basic formulation

Variational estimation is a step of the cycling algorithm intended for improving ‘shapes’ of certain unknown distributed variables, and for reducing the impact of other unknown distributed variables considered as nuisance parameters. It is based on minimization of (29) with respect to $X_a \subset X$

$$X'_a = \operatorname{argmin}_{X_a} J_1(X_a, X \setminus X_a),$$

under box constraints

$$X_a^{lb} < X'_a < X_a^{ub}.$$

The practical way of solving minimization problem (29) involving the parameter search procedure is based on the iterative regularization method (Alifanov et al., 1996; Gejadze and Malaterre, 2017; Kaltenbacher et al., 2008). This implies that the original cost function is reformulated using the change of variables

$$\tilde{X}_a = C^{-1/2} \sigma^{-1} (X_a - X_a^*)$$

in the following form:

$$\tilde{X}'_a = \operatorname{argmin}_{\tilde{X}_a} J_1(\tilde{X}_a, X \setminus X_a), \quad (43)$$

where

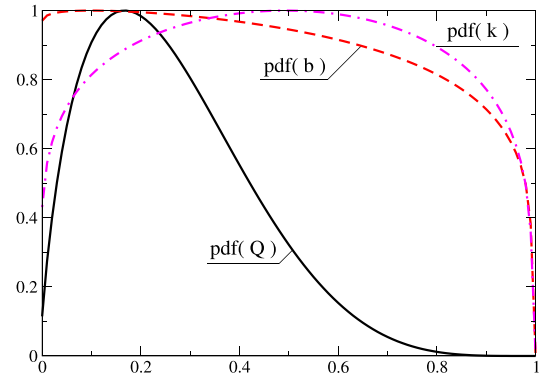


Fig. 3. Probability density function for $\rho(\bar{Q})$, $\rho(\bar{b})$ and $\rho(\bar{k})$.

$$J_1(\tilde{X}_a, X \setminus X_a) = \|\mathcal{N}_{SV}(X_a^* + \sigma C^{1/2} \tilde{X}_a, X \setminus X_a) - Y^*\|^2, \quad (44)$$

that is, without an explicit penalty term. Then, minimization is performed using a ‘regular’ minimization method (e.g. CG or quasi-Newton). Since the uniform convergence (monotonic increase of the solution norm with iterations) is expected, the iteration number serves as a regularization parameter. The box constraints are reformulated as follows

$$\frac{a-b}{2} < \tilde{X}_a < \frac{a+b}{2}, \quad (45)$$

where

$$C^{1/2} a = \sigma^{-1} (X^{ub} + X^{lb}), \quad |C^{1/2} b = \sigma^{-1} (X^{ub} - X^{lb}). \quad (46)$$

With this approach one can still use a simple box constrained minimization method, such as LBFGS-B (Byrd et al., 1995). Other technical details on the variational DA approach involving the SIC² model (SIC4DVAR) can be found in Gejadze and Malaterre (2017).

4.6.2. Control vector

Let us consider the full input set of the Saint–Venant model (8). Some components of the input vector are completely unknown, some are known approximately, some are measured directly (but not perfectly) or deduced from SWOT measurements involving another procedure. Technically, all components can be included into the control vector (active subset of the full input set) in the variational DA framework. However, to benefit from such inclusion one must know the relevant background covariance matrix. This is rarely possible in practice, so a ‘sufficient’ control vector has to be chosen. In particular, we define this vector as follows:

$$X_a = (\mathcal{C}(t), h_L(t), k_{md}(x), b(x))^T. \quad (47)$$

The explanation for this choice is as follows:

$\mathcal{C}(t)$ – the upstream discharge. It is the variable of interest, i.e. the major expected output of estimation, thus included into the control vector;

$h_L(t)$ – the downstream water surface elevation. It is an observed variable in the given idealized setup, where $h(x, t)$ is provided with a regular time step and over the spatial domain of interest. Thus, we consider $h_L(t_i) = h^*(L, t_i)$, while $h_L(t \neq t_i)$ is obtained by interpolation. In reality the observations could be irregularly distributed over the spatio-temporal domain, in which case simple interpolation would not be sufficient to recover $h_L(t)$. Thus, it is better to consider $h_L(t)$ as one of the unknowns. Included into the control vector;

$Q_0(x), h_0(x)$ – the initial conditions. For the given spatio-temporal scales have no big impact on the solution. Have to be chosen such that the initial shock does not lead to the loss of stability of the Saint–Venant solver. Not included into the control vector;

$b(x)$ – the depth of the wet bathymetry. Only the range for this variable can be guessed, e.g. $b_{min} < b(x) < 0$. Included into the control vector as a major unknown variable alongside $\mathcal{C}(t)$;

$k_{mn}(x)$ – the Strickler coefficient attributed to the minor bed or wet bathymetry. Only the range for this variable can be guessed based on physical considerations, e.g. $10 < k_{mn}(x) < 60$. However, one may expect a strong equifinality between $b(x)$ and $k_{mn}(x)$. So, it is not included into the control vector.

$k_{md}(x)$ – the Strickler coefficient attributed to the medium bed or dry bathymetry. Similarly to $k_{mn}(x)$, the range of it can be guessed based on physical considerations, e.g. $10 < k_{md}(x) < k_{mn}(x)$. If the cross-section profile for the medium bed is different from rectangular, less equifinality between $k_{md}(x)$ and $b(x)$ should be expected. Also, $k_{md}(x)$ is more likely to vary along the reach than $k_{mn}(x)$ due to change of vegetation and land cover. Included into the control vector;

$p_g^*(x)$ – medium bed or dry bathymetry. It is deduced from SWOT observations using the algorithm described in Section 2. Not included into the control vector.

4.6.3. Special constraints

The role of the variational DA step in the suggested cycling algorithm is to improve ‘shapes’ of some distributed controls, whereas their (temporal or spatial) mean values are obtained using the direct Bayesian estimator, Section 4.4. To be in agreement with this concept, the variational DA step is not allowed to change significantly the mean values of the estimated controls. Implementation of this rule gives additional integral constraints. For example, for $\mathcal{C}(t)$ one can consider the following

$$|\overline{\mathcal{C}(t)} - \overline{\hat{\mathcal{C}}(t)}| \leq \epsilon \overline{\hat{\mathcal{C}}(t)} \quad (48)$$

where $\hat{\mathcal{C}}(t)$ is the output of the Bayesian estimator given by (31), and ϵ is a constant. In the framework of iterative regularization, this constraint is implemented as an additional stopping rule for the minimization process. In numerical modeling $\epsilon = 0.1$ has been used.

4.6.4. Background covariance matrix

There is little information on the properties of the error functions in our circumstances. It is clear, however, that for each stand-alone case (particular reach of a certain river) this error has rather a systematic nature. That is why the background covariance is simply considered as a tool helping to achieve a robust uniform convergence in viable directions, rather than reach the minimum as quickly as possible.

The correlation matrix C is block-diagonal, each block being associated with one component of the control vector. In theory, the minimization process for (44) must converge to the same minimum point for any C and σ , but via different trajectories (sequences of updates). For example, the larger the correlation is, the smoother are the subsequent updates. The convergence trajectories play a very important role in solving ill-posed problems, especially those with non-uniqueness. The important thing is the relative relationship of the correlation radii and σ for different components.

Concerning the standard deviation vector σ we use the method described below. This method is rather heuristic, thus no theoretical justification is presently available. However, it performs surprisingly well in numerical tests. Consider the Modified Manning Low-Froude two-bed model (14) with the input vector

$$X = \left(h^*(x, t), \bar{k}k_1(x), k_{md}(x), \bar{b}b_1(x), p_g^*(x) \right)^T. \quad (49)$$

First, the variance $\text{Var}[Q](x, t)$ is represented using the total-effect global sensitivity indices s in the form

$$\text{Var}[Q](x, t) = s_h(x, t)\text{Var}[h] + s_k(x, t)\text{Var}[k_{md}] + s_b(x, t)\text{Var}[b],$$

where

$$\begin{aligned} s_h(x, t) &= E \left[\frac{\partial \mathcal{M}_{M2}(X)}{\partial h} \right]^2, \quad s_k(x, t) = E \left(\frac{\partial \mathcal{M}_{M2}(X)}{\partial k_{md}} \right)^2, \quad s_b(x, t) \\ &= E \left[\frac{\partial \mathcal{M}_{M2}(X)}{\partial b} \right]^2, \end{aligned}$$

and E stands for the expectation (probabilistic mean) taken over the trial plain $\{\bar{b}, \bar{k}\}$. It is also assumed that the error variance in the input variables does not depend on time or space. Next, we accept the ‘equal contribution’ principle, which means that

$$\frac{1}{3} \text{Var}[Q](x, t) = s_h(x, t)\text{Var}[h] = s_k(x, t)\text{Var}[k_{md}] = s_b(x, t)\text{Var}[b]$$

Consider, for example, the first relationship and compute its spatio-temporal mean

$$\frac{1}{3} \overline{\text{Var}[Q]} = \bar{s}_h \text{Var}[h], \quad (50)$$

where

$$\bar{s}_h = E \left[\frac{1}{LT} \int_0^T \int_0^L \left(\frac{\partial \mathcal{M}_{M2}(X)}{\partial h} \right)^2 dx dt \right]. \quad (51)$$

From (50) we obtain

$$\text{Var}[h] = \frac{\overline{\text{Var}[Q]}}{3\bar{s}_h}$$

and, finally

$$\sigma[h] = \frac{\overline{\sigma[Q]}}{\sqrt{3(\bar{s}_h)^{1/2}}}. \quad (52)$$

Following the same logic we obtain the relationships similar to (52) for $\sigma[k]$ and $\sigma[b]$, involving \bar{s}_k and \bar{s}_b expressed via the relevant derivatives. In practice, these are computed by running the adjoint of the Modified Manning two-bed model (14). Finally, we notice that only the relative weights of different components of the control vector are important, so we can put $\overline{\sigma[Q]} = 1$. Let us note that $\sigma[\cdot]$ is a constant for each component of the control vector.

4.7. Algorithm summary

Here we provide the summary of the SIC-BVC algorithm applied for solving the discharge estimation problem in this study. A simplified flowchart is also presented in Fig. 4 to facilitate understanding of the algorithm. In practical computations just two cycles are used, only the minor bed depth shape $b_1(x)$ is updated between cycles.

Put $b^1(x) = 1$ and $k_1(x) = 1$.

Start cycles $n = 1, \dots$

• 1. Scale ‘shape’ estimates

$$b_1^n(x) = b^n(x) / \bar{b}^n \quad (53)$$

• 2. Trials step: compute cost function for different \bar{b} and \bar{k}

Define $\tilde{J}_{min} = 10^{32}$.

Bathymetry loop $i = 1, \dots, n_1$

Update $\bar{b}_i = b^{ib} - (i-1)\Delta\bar{b}$.

Generate the shape function $Q_{1,i}(t) = Q_1(1, \bar{b}_i, b_1^n(x))$ according to (19).

Friction loop $j = 1, \dots, n_2$

* Update $\bar{k}_j = k^{jb} + (j-1)\Delta\bar{k}$

* Solve the 1D constrained minimization problem using the Brent method (Brent, 1973)

$$\bar{\mathcal{C}}'_{ij} = \underset{\bar{\mathcal{C}}}{\operatorname{argmin}} J_0(\bar{\mathcal{C}}, Q_{1,i}, \bar{k}_j, k_1^n, \bar{b}_i, b_1^n), \bar{\mathcal{C}}^{lb} \leq \bar{\mathcal{C}}'_{ij} \leq \bar{\mathcal{C}}^{ub} \quad (54)$$

keeping in memory both $\bar{\mathcal{C}}'_{ij}$ and the corresponding values of the cost function $J_{0,(ij)}$

End friction loop

Compute \tilde{J}_i according to (39).

If $\tilde{J}_i < \tilde{J}_{min}$ then $\tilde{J}_{min} = \tilde{J}_i$.

Check stopping criteria:

if $\tilde{J}_i > 10\tilde{J}_{min}$ then put $\bar{b}^{lb} = \bar{b}_{i-1}, n_1 = i - 1$; exit bathymetry loop.

End bathymetry loop

Define the global minimum $\hat{J}_0 = \tilde{J}_{min}$.

• 3. Direct Bayesian estimation step: computing $\hat{\mathcal{C}}(t), \hat{b}(x)$, and $\hat{k}(x)$

Compute $\mathcal{C}_{pr}(t)$ according to (34).

Optimal regularization parameter search loop: $l = -l_1, l_2$

For given $\alpha = m/2^l$ compute $\hat{\mathcal{C}}(t)$ according to (31), $\operatorname{Var}\{\mathcal{C}(t)\}$ according to (38), $\hat{b}(x)$ and $\hat{k}(x)$ according to (37, 36) and, finally, $J_{0,l}(\hat{\mathcal{C}}(t), \hat{k}, k_1, \hat{b}, b_1)$ according to (22) involving

$$X_l = \left(\hat{\mathcal{C}}(t), h_L^*(t), \hat{k}(x), \hat{b}(x)w^*/w^*(x), p_g^*(x) \right)^T, \quad x \in [0, L], t \in [0, T].$$

Compute the probabilistic (Mahalanobis) distance between the prior $\mathcal{C}_{pr}(t)$ and posterior $\mathcal{C}(t)$:

$$s_l = \int_0^T \frac{(\hat{\mathcal{C}}(t) - \mathcal{C}_{pr}(t))^2}{\operatorname{Var}\{\mathcal{C}(t)\}} dt. \quad (55)$$

End l-loop

Build parametric curve (analogue to L-curve) using points $\{J_{0,l}(\cdot)/\hat{J}_0 - 1, s_l\}$, $l = -l_1, l_2$, and detect the ‘corner’. The corresponding

$l = l^*$ gives the optimal value $\alpha^* = m/2^{l^*}$.

For given $\alpha = \alpha^*$:

- compute Bayesian posterior estimates $\hat{\mathcal{C}}(t), \hat{b}(x)$ and $\hat{k}(x)$
- construct priors for variational DA, i.e. the background vector X_a^* for (44)
- compute weights $\sigma[h]$, $\sigma[b]$ and $\sigma[k_{md}]$ for variational DA

• 4. Defining constraints for variational DA

For the control vector X_a , defined in (47), compute the box constraints for the transformed vector \tilde{X}_a using (45)-(46), given $\sigma[\cdot], C$ and the local bounds X_a^{lb} and X_a^{ub} (see Section 5a).

• 5. Variational DA step

Update X_a^* – the best available approximation of the control vector X_a , by solving the minimization problem (43) for the cost function (44), subjected to box constraints (45)-(46), using the LBFGS-B algorithm. In formulas (43)–(46) we use:

$$X \setminus X_a = \left(Q_0(x), h_0(x), \hat{k}(x), p_g^*(x) \right)^T, \quad (56)$$

$$X_a = \left(\mathcal{C}(t), h_L(t), k_{md}(x), b(x) \right)^T, \quad (57)$$

$$X_a^* = \left(\hat{\mathcal{C}}(t), h_L^*(t), \hat{k}(x), \hat{b}(x) \right)^T. \quad (58)$$

Stop iterations if condition (48) is violated.

End cycles (n-loop)

4.8. Generalized discharge estimator

The presented algorithm includes several steps of different complexity. The least expensive discharge estimate can be obtained by (34)-(35), i.e. without running the Saint-Venant model. A significantly more expensive estimate is given by Eqs. (31)–(33), which involve the likelihood function (matrix). Here one must compute the cost function (22) for different \bar{b} and \bar{k} , which implies running the Saint-Venant model up to $n_0 \times n_1 \times n_2$ times, where n_0 is the number of minimization steps

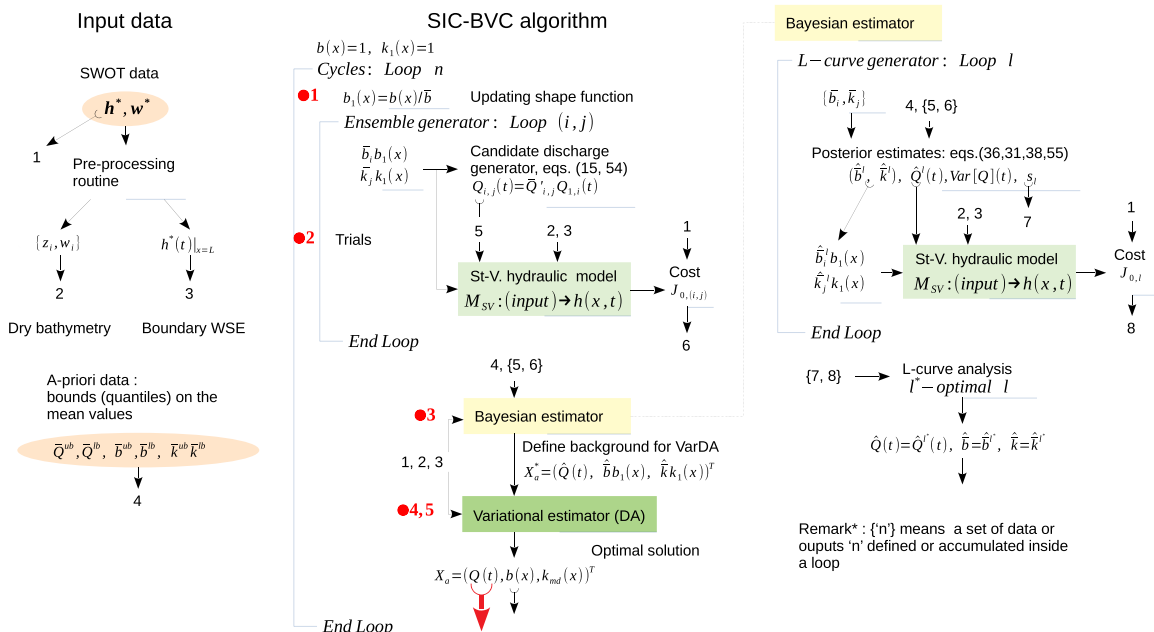


Fig. 4. SIC-BVC algorithm: flowchart.

allowed for the 1D minimization by the Brent algorithm ($n_0 = 10$ is used in this study). This step is computationally expensive, however quite straightforward to implement and perfectly scalable. The most complex step is the variational DA, which requires the adjoint of the Saint–Venant solver, and substantial memory for keeping the model’s evolution trajectory. The latter could impose a strong limitation, given that the DA period can cover years of observations.

Given a possible need of producing the discharge estimates in the global scale and in close-to-real time regime, one may suggest the estimator in the form:

$$\widehat{\mathcal{Q}}(t) = \frac{1}{\|\mathcal{C}\|} \sum_{i=1}^{n_1} \sum_{j=1}^{n_2} \mathcal{Q}_{MI,(i,j)}(t) \mathcal{L}^+[i,j] \rho(\overline{Q}_{MI,(i,j)}) \rho(\overline{b}_i) \rho(\overline{k}_j), \quad (59)$$

where

$$\mathcal{C} = \sum_{i=1}^{n_1} \sum_{j=1}^{n_2} \mathcal{L}^+[i,j] \rho(\overline{Q}_{MI,(i,j)}) \rho(\overline{b}_i) \rho(\overline{k}_j), \quad (60)$$

and $\mathcal{L}^+[\cdot]$ is a generalized likelihood function (matrix) defined as follows:

$$\mathcal{L}^+[i,j] = \mathcal{L}[J_{0,(i,j)}, \widehat{J}_0, \alpha^*] \frac{\overline{\mathcal{Q}}'_{ij}}{\overline{Q}_{MI,(i,j)}} \frac{\rho(\overline{\mathcal{Q}}'_{ij})}{\rho(\overline{Q}_{MI,(i,j)})}. \quad (61)$$

The above formulation is obtained as a result of simple manipulations with Eqs. 34,35. In (59), the product

$$\rho^* = \rho(\overline{Q}_{MI,(i,j)}) \rho(\overline{b}_i) \rho(\overline{k}_j)$$

can be interpreted as a ‘prior’ PDF, and

$$\mathcal{L}^+[i,j] \rho^*$$

as a ‘posterior’ PDF of the integrated Modified Manning model output $Q_{MI,(i,j)}(t)$. Here, the terms ‘prior’ and ‘posterior’ are used rather conventionally, since $\overline{Q}_{MI,(i,j)}$ is already conditioned on observations $h^*(x, t)$, according to Eqs. 20,21.

The advantage of representation (59)-(61) is that any currently available likelihood function can be used for the real-time discharge estimation, including the trivial case $\mathcal{L}^+[i,j] = 1$, which gives the ‘prior’ estimate according to (34)-(35). The likelihood itself can be updated independently and retrospectively, subjected to availability of computational resources. Besides, the spatial interval where $Q_{MI}(t)$ is defined does not need to be limited to the initial part of the reach $[0, \delta < L]$, but may include any subinterval from $[0, L]$.

A few examples of the ‘prior’ and ‘posterior’ PDFs, as well as the likelihood functions are presented in Fig. 5. This figure provides a good illustration on how the Bayesian estimator works. The results are typical for the PEPSI testing set. One can see that the ‘prior’ PDF covers quite a significant part of the trial plane $\{\overline{b}, \overline{k}\}$, whereas the area covered by the ‘posterior’ PDF is comparatively smaller. This means the uncertainty is reduced due to assimilation of observations into the Saint–Venant model. Let us remember that the ‘posterior’ PDF is the product of the ‘prior’ and the likelihood function, which depends on the cost function. One can observe that in some cases (e.g. ArialKhan, Mississippi Int, Seine Us) the likelihood function has no distinctive maximum point. This justifies using as an estimate the expectation of the posterior PDF, rather than its mode (minimum of the cost function). An exceptional case is Seine US, where the area of the nearly equal likelihood actually overlaps the area covered by the ‘prior’ PDF. This is an exhibition of the extreme ill-posedness/equifinality.

4.9. Direct Bayesian estimation algorithm: L-curve

At step 3 of the algorithm (‘Direct Bayesian estimation’) the optimal value of parameter α is sought using the L-curve approach. Originally,

this approach was developed for the classical Tikhonov regularization method, where the regularization parameter is a multiplier to the penalty term. It has been proved in Hansen and O’Leary (1993) that for a linear control-to-observation operator the value of the penalty term is a monotonically decreasing function of the residual norm with a distinctive ‘corner’. The optimal parameter value is the one which corresponds to this corner.

In our method, however, there are differences to the classical case. First, parameter α is placed inside the likelihood. Second, as a function of the residual norm the probabilistic distance (55) is considered. Finally, the Saint–Venant model is nonlinear. As a result, one may encounter the L-curve shapes which does not follow the expected regular behavior. Several examples are shown in Fig. 6. Two cases in the upper part of the figure (Cumberland and Seine, PEPSI-1) represent the shapes which have been encountered in testing most frequently. In the Cumberland case one can see a monotonically decreasing function, however without a distinctive corner. In this case, the optimal parameter corresponds to the point where the local derivative is equal to the average slope. In contrast to the previous case, in the Seine case a very distinctive corner is observed, however the behavior of the curve is not regular. In particular, the ‘edge effect’ can be seen. It has been found that this effect is usually related to the truncation of the bathymetry loop (see remark in Section 4.4), and disappears when the range of \overline{b} is sufficient. Two cases in the lower part (Seine DS and Seine US, PEPSI-2) represent irregular cases, which constitute the minority. However, these are presented to demonstrate that an automated search for the optimal parameter may not be easy. Presently, this is done via an expert assessment.

5. Validation procedure

5.1. General description, performance metrics and constraints

The developed algorithm has been validated on the PEPSI testing set. For each ‘case’, i.e. a selected stretch of a river, the SWOT-type observations and the reference ‘true’ discharge have been provided to the members of the SWOT DAWG, as well as the corresponding Q_{WBM} . Let us mention again that Q_{WBM} represents the mean discharge over the historical period from 1961 to 2010 with no relation to the testing period.

In the presented method we introduce some additional constraints of a very general nature. Concerning the mean Strickler coefficient \overline{k} , we assume it ranges from 10 to 60 (0.0167 to 0.1 for Manning), which is a reasonable assessment for natural rivers (Barnes, 1967). Concerning the mean wet bathymetry depth \overline{b} , we assume it changes from zero to $-20m$. This should be true for the majority of rivers, except very large ones which are generally better known. The PDF of these parameters is nearly uniform. Concerning the mean upstream discharge $\overline{\mathcal{Q}}$, we assume it belongs to the β -distribution with the mode at Q_{WBM} , the lower bound $Q_{WBM}/5$ and the upper bound $5Q_{WBM}$. This gives a sufficiently wide interval for $\overline{\mathcal{Q}}$ to vary. Such highly skewed distributions are often used in hydrology to characterize the rainfall. Since the river discharge is a derivative of the rainfall over the catchment, this choice of PDF seems relevant. The local bounds X_a^{lb} and X_a^{ub} used at the variational DA step are

$$0 < \mathcal{Q}(t) < 2\widehat{\mathcal{Q}}(t),$$

$$h_L^*(t) - 1m < h_L(t) < h_L^*(t) + 1m,$$

$$10 < k_{md}(x) < \widehat{k}(x),$$

$$2\widehat{b}(x) < b(x) < 0.$$

These are consistent with constraints suggested for the mean values.

Despite the fact that the observations have been generated numerically, this is not an identical twin experiment setup. We do not know which models have been used for each case, what values of numerical

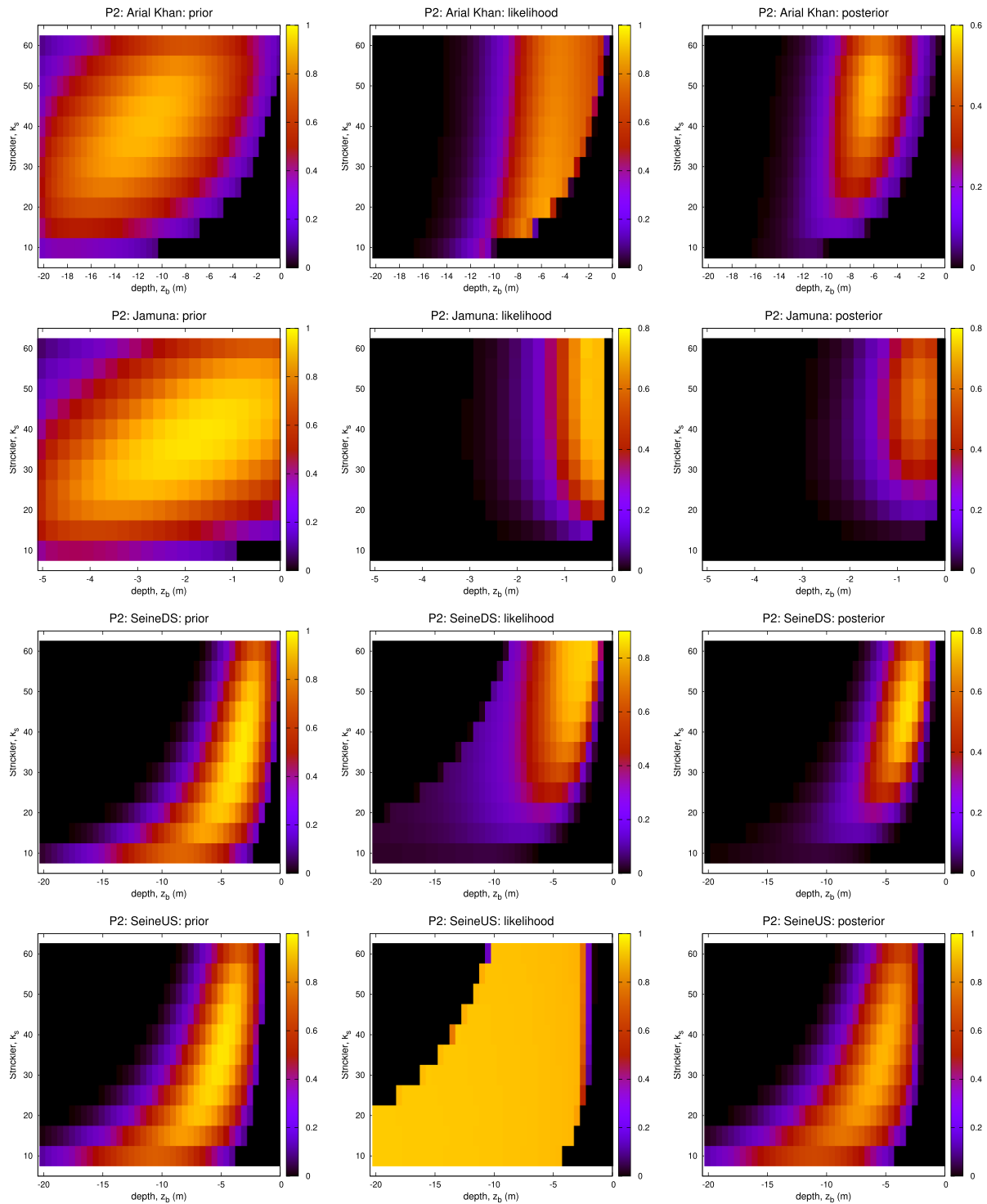


Fig. 5. Prior PDF (left), likelihood function (center) and posterior PDF (right).

parameters (for example, discretization steps) have been taken, what interpretation of the bed geometry has been accepted. For PEPSI-1, we corrupt observations by adding the Gaussian noise with zero expectation and a given variance (as in Durand et al., 2016). For PEPSI-2, the datasets without noise and including noise are directly provided, called ‘ideal’ and ‘uncertainty’ sets, respectively. For the latter, the noise is generated by means of a specially developed model, based on understanding of errors arising in the measuring instrument due to the methodology of collecting the primary data (Durand et al., 2020; Fransson et al., 2021).

Let $y(t)$ be an arbitrary function of time. In order to compare this function with a given reference value $y_{ref}(t)$ the following metrics are used:

- normalized bias (NBIAS):

$$NBIAS = \frac{\bar{y}}{\bar{y}_{ref}} - 1$$

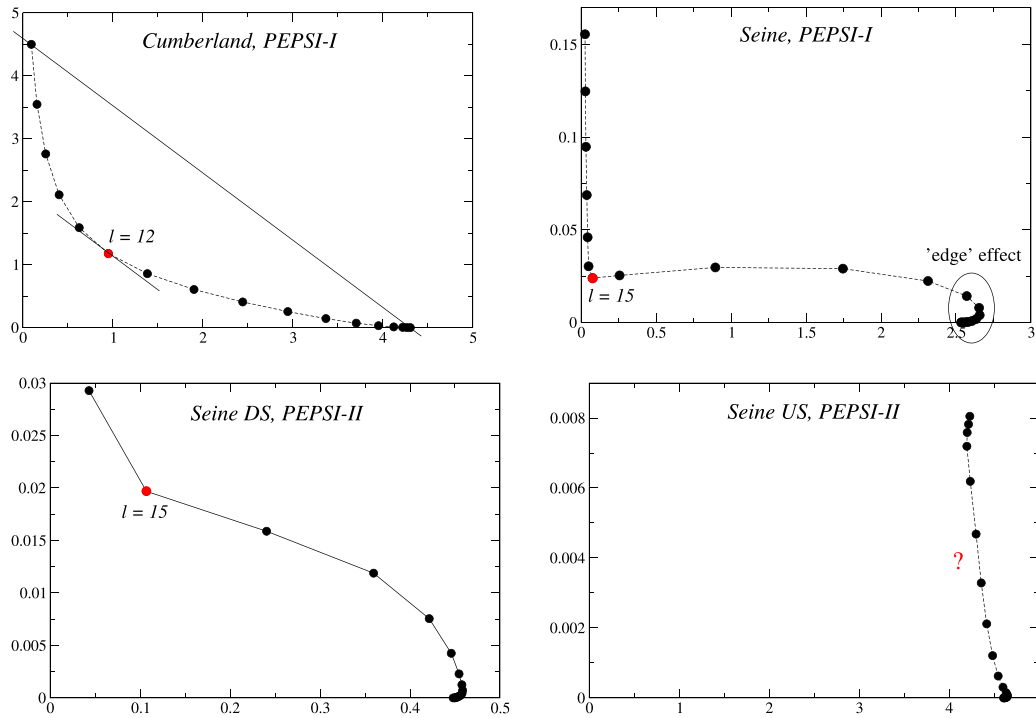


Fig. 6. L-curve examples.

- Nash–Sutcliffe efficiency (NSE):

$$\text{NSE} = 1 - \frac{1}{\text{var}[y_{\text{ref}}(t)]} \frac{1}{T} \int_0^T (y(t) - y_{\text{ref}}(t))^2 dt$$

- relative root mean square error (RRMSE):

$$\text{RRMSE} = \left(\frac{1}{T} \int_0^T \left(\frac{y(t)}{y_{\text{ref}}(t)} - 1 \right)^2 dt \right)^{1/2}$$

- normalized root mean square error (NRMSE):

$$\text{NRMSE} = \frac{1}{\bar{y}_{\text{ref}}} \left(\frac{1}{T} \int_0^T (y(t) - y_{\text{ref}}(t))^2 dt \right)^{1/2}$$

- normalized root mean square error invariant (NRMSEI): the same as above with scaling factor

$$\bar{y}_{\text{ref}} = (\bar{y}_{\text{ref}}^2)^{1/2}.$$

RRMSE has been used in PEPSI-1 tests (Durand et al., 2016). This metric has later been abandoned in favor of NBIAS, NRMSE and NSE in PEPSI-2 tests (Frasson et al., 2021). Here we provide RRMSE only to enable comparison of our results on PEPSI-1. Concerning NRMSE used in Frasson et al. (2021), we notice that it is not very suitable for signals characterized by long periods of low variability (e.g. Brahmaputra). Thus, we suggest another metric called NRMSEI (where I stands for ‘invariant’). Again, for comparison we present our results in terms of NRMSE. Let us note that NSE is not a useful performance criteria when the variability of the function is small against its mean value.

In validation we compare either the upstream discharge $y(t) := \mathcal{Q}(t)$, or the spatially averaged (reach-averaged) discharge

$$y(t) := \bar{Q}(t) = \frac{1}{L} \int_0^L Q(x, t) dx, \quad (62)$$

where $Q(x, t)$ is the Saint–Venant solution (9), given the model input vector as follows: after the direct Bayesian estimation step (step 3)

$$X = \left(\hat{\mathcal{Q}}(t), h_L^*(t), Q_0(x), h_0(x), \hat{k}(x), \hat{k}(x), \hat{b}(x), p_g^*(x) \right)^T, \quad (63)$$

and after the variational DA step (step 5):

$$X = \left(\mathcal{Q}'(t), h_L'(t), Q_0(x), h_0(x), \hat{k}(x), k_{md}'(x), b'(x), p_g^*(x) \right)^T. \quad (64)$$

One can see that $\bar{Q}(t)$ depends on the upstream discharge $\mathcal{Q}(t)$, but also on the estimates of $b(x)$, k_{mn} , $k_{md}(x)$ and $h_L(t)$.

6. Results

¹ The results of solving the discharge estimation problem are generalized in terms of the performance metrics (see Section 5.1), which are presented in Tables 1,2 and visualized using the box-plots in Fig. 7–10. First, in Fig. 7 the advantage of using the posterior expectation instead of the posterior mode (i.e. the optimal solution) is demonstrated. Here we compare the accuracy of the ‘prior’ (34), the posterior expectation (31) and the posterior mode of the upstream discharge after Step 3 of the Algorithm. The mode is defined as follows:

$$\mathcal{Q}'(t) = \mathcal{Q}'_{i,j} Q_{i,j}(t),$$

¹ The complete results of solving the discharge estimation problem can be presently downloaded from: https://www.dropbox.com/s/6wmji9wv5g0vx71/discharge_P1.tar.gz?dl=0, https://www.dropbox.com/s/lzw1jksl66ut0xi/discharge_P2.tar.gz?dl=0.

where

$$(i', j') = \underset{ij}{\operatorname{argmax}} \mathcal{L}[J_{0,(i,j)}, \hat{J}_0, \alpha^*] \rho(\bar{\mathcal{C}}_{ij}, \bar{b}_i, \bar{k}_j).$$

Let us note that what we call ‘prior’ here is an estimate already conditioned on observations $h^i(x, t)$ via \mathcal{M}_{MI} model. Moreover, it incorporates some results of running the Saint–Venant model, since the range of the minor bed depth \bar{b} could have been reduced during the depth loop, see remark in Section 4.4. Nevertheless, this is the simplest and the least expensive useful output of our method. Thus, it is worth comparing this estimate with more advanced and expensive ones.

One can conclude looking at Fig. 7 that, on average, the expectation is a noticeably better estimate of the upstream discharge than the mode, for all metrics. This proves the key idea of our method: evaluate the posterior expectation of the temporal/spatial means of the distributed parameters rather than the optimal values (modes). Secondly, in average, the accuracy of the ‘prior’ seems to be comparable to the accuracy of the mode, given a reasonable range for \bar{b} is defined. Since the ‘prior’ is much less computationally expensive than the optimal solution, this gives an interesting hint on the possible future developments.

Next, Fig. 8 shows the performance of the full Algorithm, with metrics being computed using the spatially averaged discharge, according to (62)–(64). Here we present the averaged performance: A – after 1 cycle, PEPSI-1/2; B – after 2 cycles, PEPSI-1/2; C – after 2 cycles, PEPSI-2 testing set only. Case C is considered separately to facilitate comparison with the results reported in Frasson et al. (2021). A drop in the estimation quality in comparison to the complete PEPSI set is due to the presence of the short duration cases in PEPSI-2 ($T = 11$ days, see Table 2), for which the estimation accuracy is usually less good than for the long duration cases. One can see that the accuracy of the spatially-averaged discharge estimate is improved after the second cycle. This result confirms the idea of the Bayesian Variational estimation cycles, where the information exchange is limited to the updated shape functions ($b_1(x)$ in our case). Clearly, running another cycle means the proportional rise of the computational cost.

Next, in PEPSI-2 we investigate how the accuracy of the estimated discharge depends on the observation period (period between snapshots, satellite revisiting period). This period is considered constant, so one can equally speak in terms of the snapshot frequency. It is obvious that when the snapshot frequency drops, certain frequencies in the water surface temporal evolution become unobservable. These are naturally lost in the final solution for $\mathcal{C}(t)$. Thus, the performance metrics largely depend on the frequency content of the discharge hydrograph. That is why the metrics are **computed at the observation instants only**, similarly to Frasson et al. (2021). As before, the metrics are based on the spatially averaged discharge. Only the ‘long duration’ cases are included in this test (overall 19 cases, see Table 2). The results are presented in Fig. 9. Here, one can see that: a) the estimation accuracy degrades when the snapshot frequency drops; b) this degradation occurs mainly during the transition from 1-day to 4-days period; c) further increase of the period (from 4 to 10 days) does not lead to any noticeable degradation, at least in terms of the NSE and NRMSE metrics. The likely explanation of this behavior may be related to the fact that all test cases considered in this paper have the characteristic time less than 2 days. However, if the observation frequency is less than the characteristic frequency of the dynamical system, no benefit from using the unsteady model of this system could be attained. This is the difference between the 1-day and (4–7–10)-day cases. Given that the SWOT satellite revisiting period will generally range from 5 to 10 days, it makes sense to use the steady-state SV model instead of the unsteady SV model (which is also much less expensive computationally). On the other hand, it is possible to imagine that in the future the information may come from a several satellites, so the observation period could be significantly reduced.

In the previously described results involving PEPSI-2 the exact SWOT observations from the ‘ideal’ testing set have been used. In the final tests

we have used the noisy observations from the ‘full uncertainty’ testing set. The results are presented in Fig. 10. One can see that the box-plot medians with and without noise (A and B, respectively) remain nearly the same, whereas the box size (distance between 1st and 3rd quartiles of the sample) is even reduced when using the noisy data. Moreover, NBIAS is smaller in this case. While these results look somewhat encouraging, the number of test cases including noise is too small to draw any definitive conclusions.

There are several cases within PEPSI-1/2 where the true discharge does not fit into the accepted interval $[Q_{WBM}/5, 5Q_{WBM}]$, see Tables 1, 2. These are Tanana (PEPSI-1), and MiddleRiver, Olentangy, SanJoaquin 2, Padma (all PEPSI-2). All cases except Padma are the ‘short period’ cases (12 days) and represent the tails of the box-plots. As a rule, if the likelihood function has no distinctive ‘bell’, the estimate is strongly dominated by the prior, see upper and mid plots at Fig. 12 for example. Here, the likelihood function has a flat plateau covering most of the trial plane and, subsequently, the posterior PDF is not too different from the prior PDF. Thus, the estimation accuracy is totally determined by the quality of the prior PDF (Q_{WBM} plus bounds on $\bar{\mathcal{C}}$ defined via Q_{WBM} using (42)). For example, this quality is satisfactory in the Grant Line Canal case, and unsatisfactory in the MiddleRiver case, with the corresponding estimation results. In contrast, the estimation accuracy for Padma is much better than one may expect given the accuracy of the prior mean discharge ($Q_{WBM}/Q_{truth} = 0.072$). There are two reasons for that. First, the mean discharge prior PDF is originally skewed toward larger discharge values. Second, the likelihood function, see the bottom plot at Fig. 12, has a distinctive ridge at $\bar{b} = -5m$. This likelihood transforms the prior PDF in a way which implies an additional discharge increase. Overall, the plots like those presented in Fig. 5 or Fig. 12 are useful for explaining the estimation results.

By request of Reviewers we additionally present some materials which facilitate comparison of SIC-BVC to other SWOT DAWG algorithms. First, Fig. 11 shows the performance of SIC-BVC, MetroMan and HiVDI algorithms in terms of NSE, NRMSE and NBIAS metrics. We also provide Table 3, which contains the values of NRMSE achieved by our method and by MetroMan, HiVDI, GeoBam and SADS, for each case from the PEPSI-II testing set.

Considering Fig. 11 one can conclude that the suggested SIC-BVC algorithm yields noticeably more accurate and more stable estimates than either MetroMan or HiVDI. The latter two are, in turn, the most accurate among all SWOT DAWG algorithms. Saying that we have to underline that a straightforward comparison of the results may not be fully legitimate. One thing is that the results by SWOT DAWG algorithms over the PEPSI-II testing set were obtained in a ‘blind’ experiment, which means no information about the reference (‘true’) discharge was available to tune the algorithms. In contrast, this information was available to us at the algorithm development stage and, therefore, could have influenced some of the design solutions implemented. Other points are rather technical. First, the SWOT DAWG algorithms work at the reach level, then the discharge estimates are averaged over all ‘good’ reaches. In the SIC-BVC algorithm we are looking for a longest sequence of adjacent ‘good’ reaches to define a continuous spatial domain where the hydraulic model is set up. Therefore, if there exist ‘good’ reaches outside this sequence, these are excluded from our analysis. Second, our results include the ArialKhan case, which means that the boxplots for the MetroMan and HiVDI performance presented in our paper in Fig. 11 may slightly differ from those presented in Frasson et al. (2021).

While the actual impact of the mentioned factors is difficult to access, we strongly believe it may not change the overall picture.

7. Conclusions

Our recent experience with the variational DA method applied for estimating the river discharge in the SWOT mission context has confirmed that the problem of simultaneous estimation of the upstream

Table 1
Performance, PEPSI-1.

	Case	T(days)	Q_{ruhh}	Q_{wbm}	NBIAS	RRMSE	NRMSE	NRMSI	NSE
1	Connecticut	160	634.23	394.11	-0.012	0.120	0.179	0.139	0.951
2	Cumberland	160	905.43	511.39	0.102	0.399	0.161	0.128	0.957
3	Ganges	365	12155.68	10943.69	-0.212	0.187	0.350	0.240	0.891
4	Garonne US	365	155.88	54.68	-0.075	0.223	0.079	0.067	0.984
5	Garonne DS	365	482.34	528.48	-0.170	0.122	0.177	0.145	0.936
6	Kanawha	365	626.17	305.00	-0.215	0.218	0.254	0.212	0.852
7	Mississippi DS	160	15190.27	8928.31	-0.394	0.457	0.395	0.373	-0.294
8	Mississippi US	160	5412.42	3383.44	-0.310	0.365	0.310	0.293	0.220
9	Ohio	250	4001.73	2459.92	0.131	0.243	0.139	0.109	0.969
10	Platte	24	151.52	56.86	-0.136	0.928	0.284	0.231	0.841
11	Po	365	1499.88	841.81	-0.274	0.423	0.283	0.207	0.908
12	Sacramento DS	152	272.01	377.00	0.171	0.148	0.285	0.239	0.808
13	Sacramento US	302	206.19	377.00	-0.090	0.134	0.132	0.112	0.955
14	Seine	360	300.29	205.54	-0.111	0.101	0.147	0.126	0.940
15	Severn	90	105.09	104.85	0.268	0.866	0.275	0.187	0.935
16	StLawrence DS	140	9606.80	9586.54	0.282	0.329	0.322	0.320	-8.050
17	StLawrence US	140	9606.80	7753.74	-0.124	0.132	0.127	0.126	-0.398
18	Tanana	98	1443.00	344.77	-0.718	0.725	0.721	0.714	-24.68
19	Wabash	160	972.89	565.30	-0.183	0.403	0.226	0.189	-0.878

Table 2
Performance, PEPSI-2.

	Case	T(days)	Q_{ruhh}	Q_{wbm}	NBIAS	NRMSE	NRMSI	NSE
20	ArialKhan	360	808.06	2459.00	0.438	0.471	0.315	0.820
21	AshSlough	12	38.47	36.06	0.160	0.186	0.169	0.845
22	BerendaSlough	12	16.04	36.06	0.236	0.364	0.320	0.552
23	Brahmaputra	105	1982.82	5162.40	0.332	0.527	0.214	0.945
24	ChowchillaCan	12	21.67	36.21	0.280	0.308	0.146	0.973
25	FresnoRiver	12	52.12	45.95	-0.052	0.088	0.081	0.957
26	GrantLineCan	12	212.25	243.76	0.553	0.565	0.549	-4.415
27	IowaRiver	365	158.11	147.00	0.127	0.174	0.114	0.977
28	Jamuna	250	22024.50	16623.00	-0.130	0.140	0.106	0.973
29	Kushiyara	365	1170.53	2133.00	-0.149	0.206	0.149	0.954
30	MariposaBypass	12	108.33	75.57	-0.062	0.120	0.111	0.920
31	MercedRiver	12	94.64	75.57	-0.001	0.190	0.176	0.789
32	MiddleRiver	12	24.44	171.76	7.907	8.151	7.863	-889.2
33	Mississippi In	160	5480.35	2459.00	-0.306	0.311	0.294	0.185
34	Missouri DS	480	923.55	498.00	-0.274	0.298	0.268	0.621
35	Missouri MS	480	1016.97	498.00	-0.382	0.420	0.370	0.388
36	Missouri US	480	1032.98	498.00	-0.400	0.450	0.393	0.346
37	Ohio Section 1	220	1604.93	2459.00	0.406	0.477	0.367	0.668
38	Ohio Section 2	220	2316.96	2459.00	0.017	0.055	0.044	0.995
39	Ohio Section 3	220	2703.67	2459.00	-0.103	0.151	0.120	0.962
40	Ohio Section 4	220	3419.83	2459.00	0.057	0.072	0.056	0.992
41	Ohio Section 5	220	3803.56	2459.00	0.225	0.251	0.198	0.898
42	Ohio Section 7	220	5349.49	2459.00	-0.494	0.603	0.476	0.397
43	Ohio Section 8	220	7590.86	2459.00	-0.378	0.436	0.342	0.694
44	Olentangy	12	2.64	26.35	7.563	7.603	6.241	-118.4
45	Padma	360	29444.72	2133.00	-0.358	0.472	0.361	0.687
46	SanJoaquin	12	222.29	154.96	-0.108	0.172	0.156	0.864
47	SanJoaquin 2	12	29.32	154.96	1.291	1.425	1.253	-5.927
48	Seine DS	360	300.29	205.53	-0.100	0.181	0.155	0.909
49	Seine US	360	192.72	205.53	0.329	0.372	0.314	0.655
50	Stanislaus Riv	12	105.30	154.96	0.031	0.123	0.113	0.911
51	Tuolumne Riv	12	228.58	154.96	-0.324	0.346	0.345	-27.9

discharge hydrograph and spatially distributed hydraulic parameters may have multiple solutions. In practice, this often appears in the form of a bias, which is fully dependent on the chosen priors and the background covariance matrix.

Thus, for resolving this problem, a new robust method has been developed. The method includes a separate treatment of the temporal/spatial mean values and the 'shape' functions, representing (in product) the unknown input variables. The mean values (mean upstream discharge over the full observation period, mean weighted depth of the 'wet' bathymetry and mean Strickler coefficient) are estimated using the Bayesian method as expectations over the 2-dimensional posterior PDF, whereas the 'shape' functions – using the variational DA method and the Integrated Modified Low-Froude GMS model. Looking for the

expectation instead of a mode is a key expedient to construct a robust estimator. This is due to the fact that, unlike the modes, the conditional expectation of any PDF with finite variance is unique almost surely.

The Bayesian estimation step by itself combines minimization of the cost function with respect to the mean discharge with integration over the trial plane (mean weighted depth versus mean Strickler). Besides, the novel elements include using a 'regularization' parameter, which controls the decay rate of the likelihood, rather than that of the prior PDF (the latter corresponds to the standard Tikhonov approach), plus adaptation (or generalization) of the L-curve principle for the optimal choice of this parameter.

Other important methodological findings include:

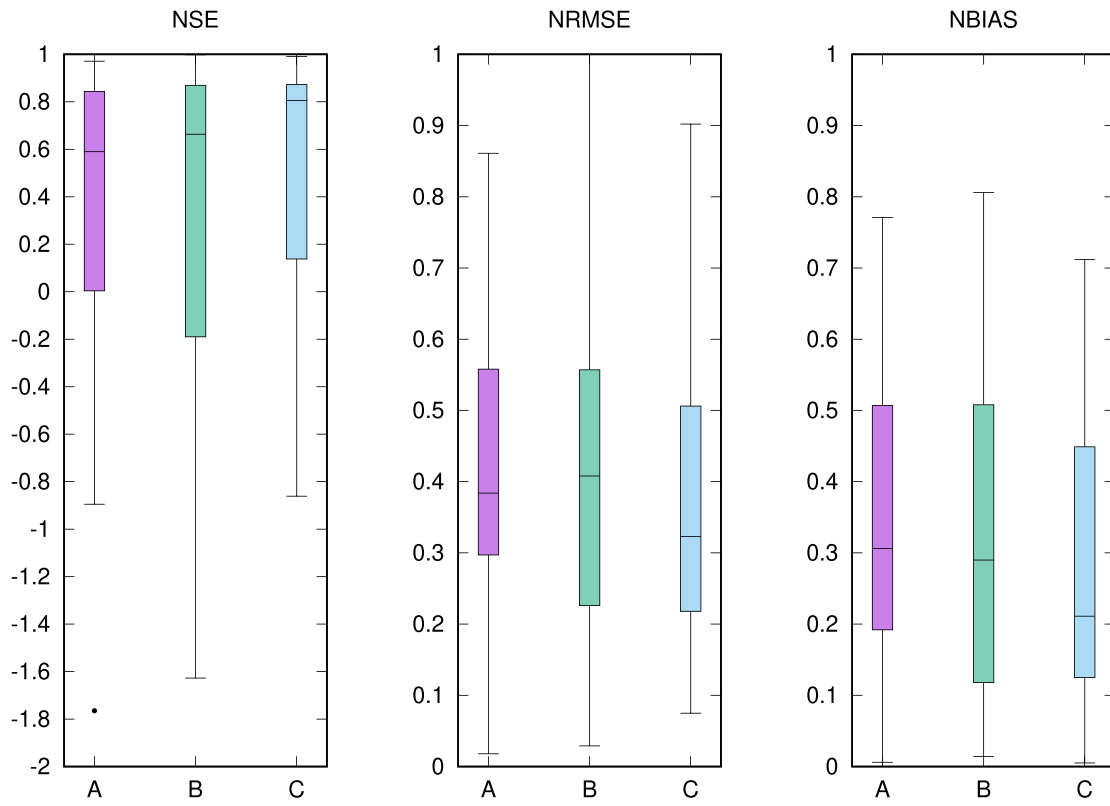


Fig. 7. Performance metrics for the upstream discharge $Q(t)$ after Step 3 at first cycle: A – ‘Prior’, B – posterior mode (optimal solution), C – posterior expectation. PEPSI-1/2.

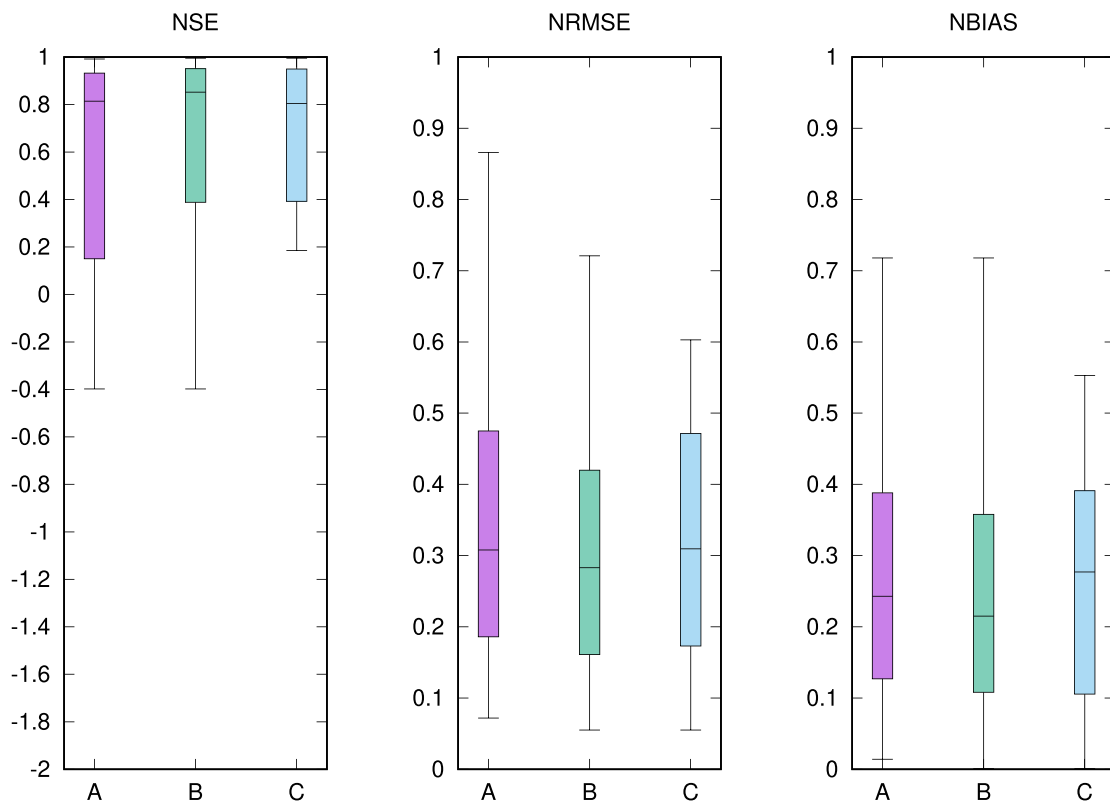


Fig. 8. Performance metrics involving the spatially averaged discharge (62): A – PEPSI-1/2 after 1 cycle, B – PEPSI-1/2 after 2 cycles, C – PEPSI-2 after 2 cycles.

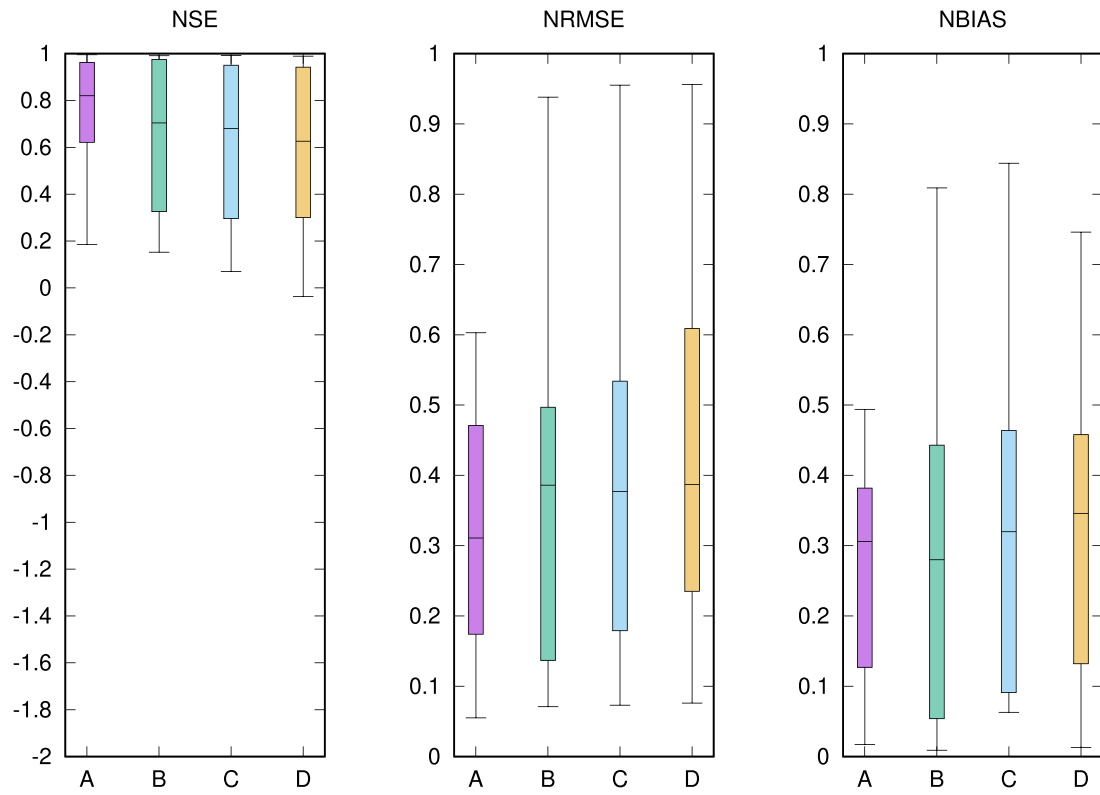


Fig. 9. Performance metrics involving the spatially averaged discharge (62), for different snapshot period: A – 1 day, B – 4 days, C – 7 days, D – 10 days. PEPSI-2.

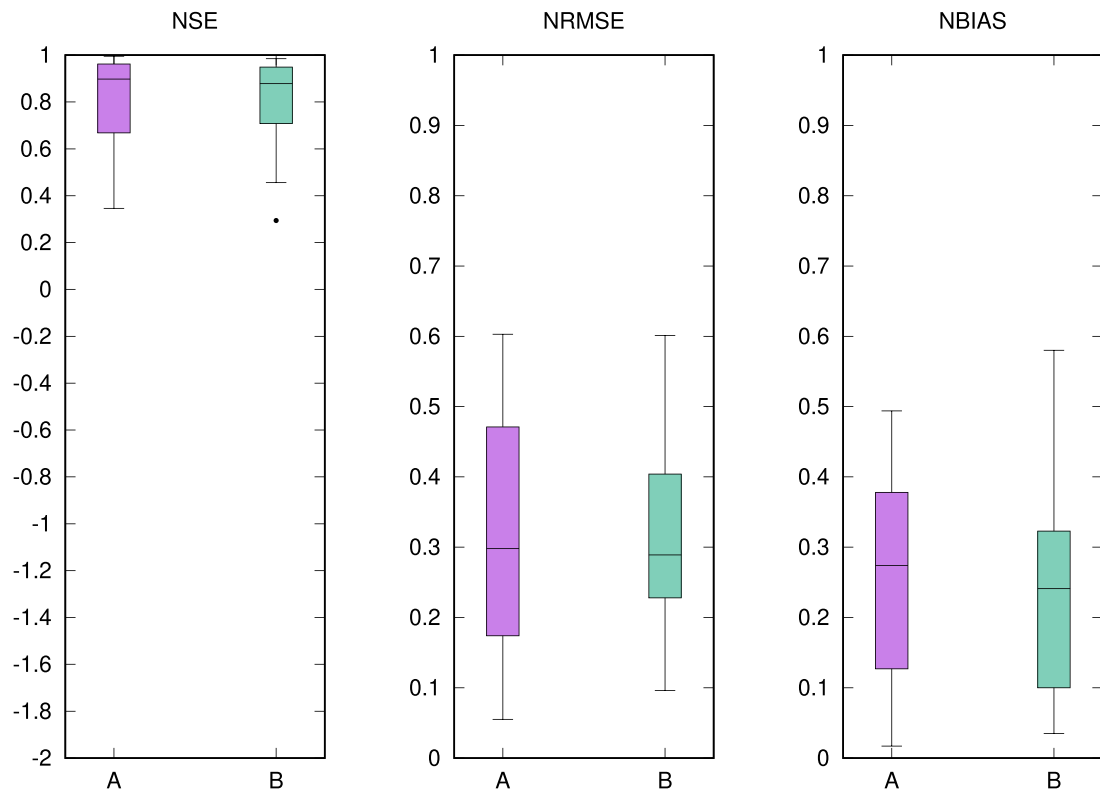


Fig. 10. Performance metrics involving the spatially averaged discharge: A – without noise and B – including noise. PEPSI-2.

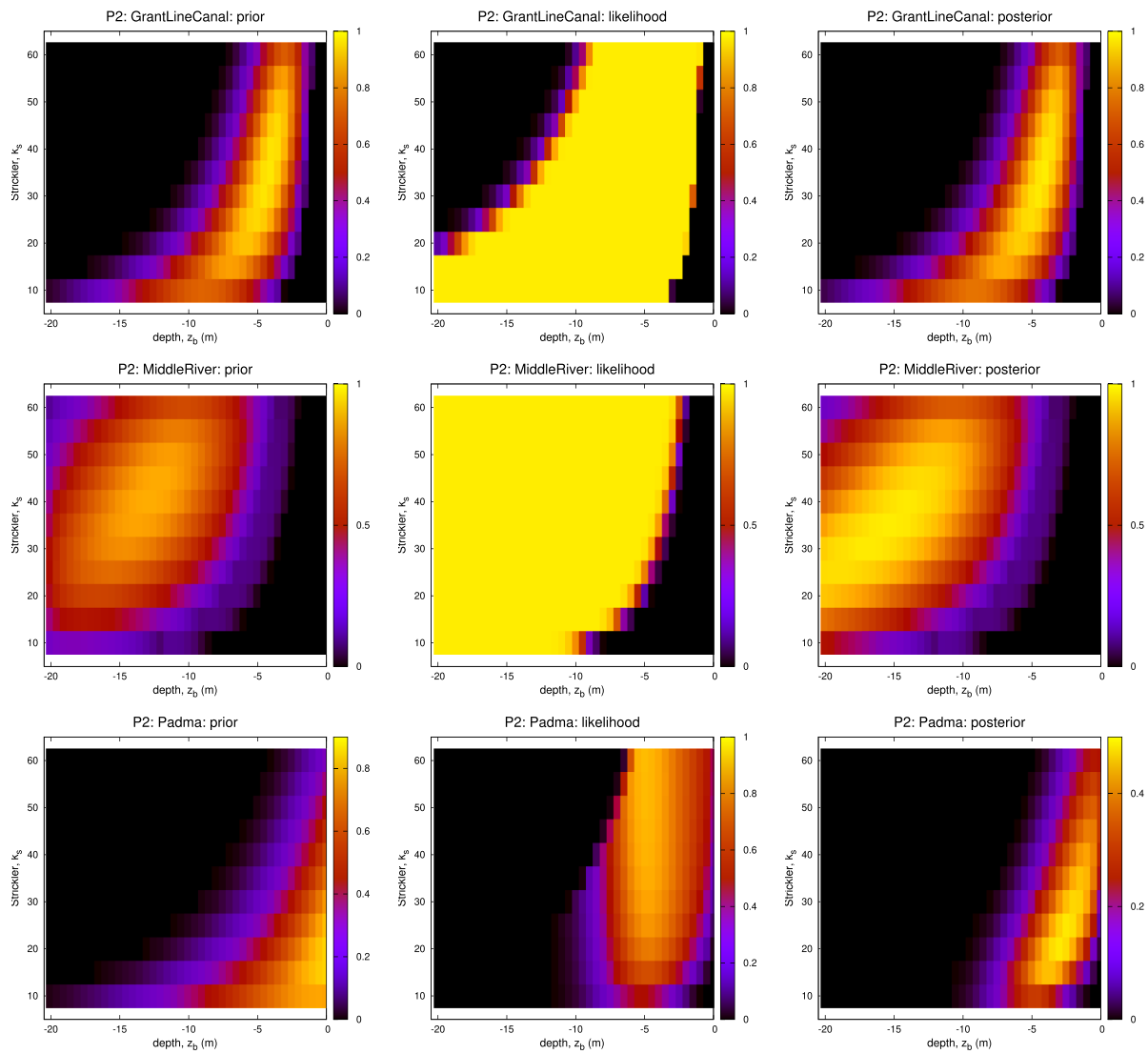


Fig. 12. Prior pdf (left), likelihood function (center) and posterior pdf (right).

- the Integrated Modified Low-Froude GMS model \mathcal{M}_{MI} , which is used for generating the hydrograph shape function (dependent on the mean depth). The generalized discharge estimator, suggested in Section 4.8 is also based on this model;
- the method for automatic construction of the simplified background covariance matrix required for the variational DA step, via the sensitivity analysis performed during the Bayesian step, as presented in Section 4.6.4.

In building the algorithm we tried to avoid any design solutions which may be considered as those introducing additional a priori information to the SWOT data. In particular, we do not use:

- a) the rating curve, neither as a downstream boundary condition, nor elsewhere;
- b) a local value of the minor bed elevation at any point along the river;
- c) any information which may come from the geomorphological classification of the area where the river case is defined.

We do use the mean discharge from the QWBM database and the following assumptions concerning the bounds:

- a) mean upstream discharge varies from $Q_{WBM}/5$ to $5Q_{WBM}$;
- b) mean weighted depth varies from 0 to $-20m$;
- c) mean Strickler varies from 10 to 60.

Let us note that the first assumption is equivalent to introducing the quantiles of the distribution of Q_{WBM} . Those were not available during this study, but could be calculated by processing the QWBM database, if the full access to it is obtained. Assumptions b) and c) are simply a common sense assumptions likely to be valid for the majority of natural rivers.

The method has been validated on the PEPSI-1/2 testing set, which has also been used by other authors in the SWOT-type data assimilation context. First to mention, the method is more robust, reliable and convenient to use than the (standing alone) variational DA method. In particular, there have been much less occurrence of critical errors due to intractable hydraulic conditions (supercritical flow, dry bed, etc). There is no longer a need to specify the priors, the background covariance matrix and the bounds, which all come from the Bayesian step (step 3 of the Algorithm). Overall, the variational DA is playing a complementary role in this algorithm, since the discharge shape function is sufficiently well reproduced using the model \mathcal{M}_{MI} described in Section 3. Of course, such a convenient shape generator may not be available in general. On the other hand, at the Bayesian step the algorithm presently requires an

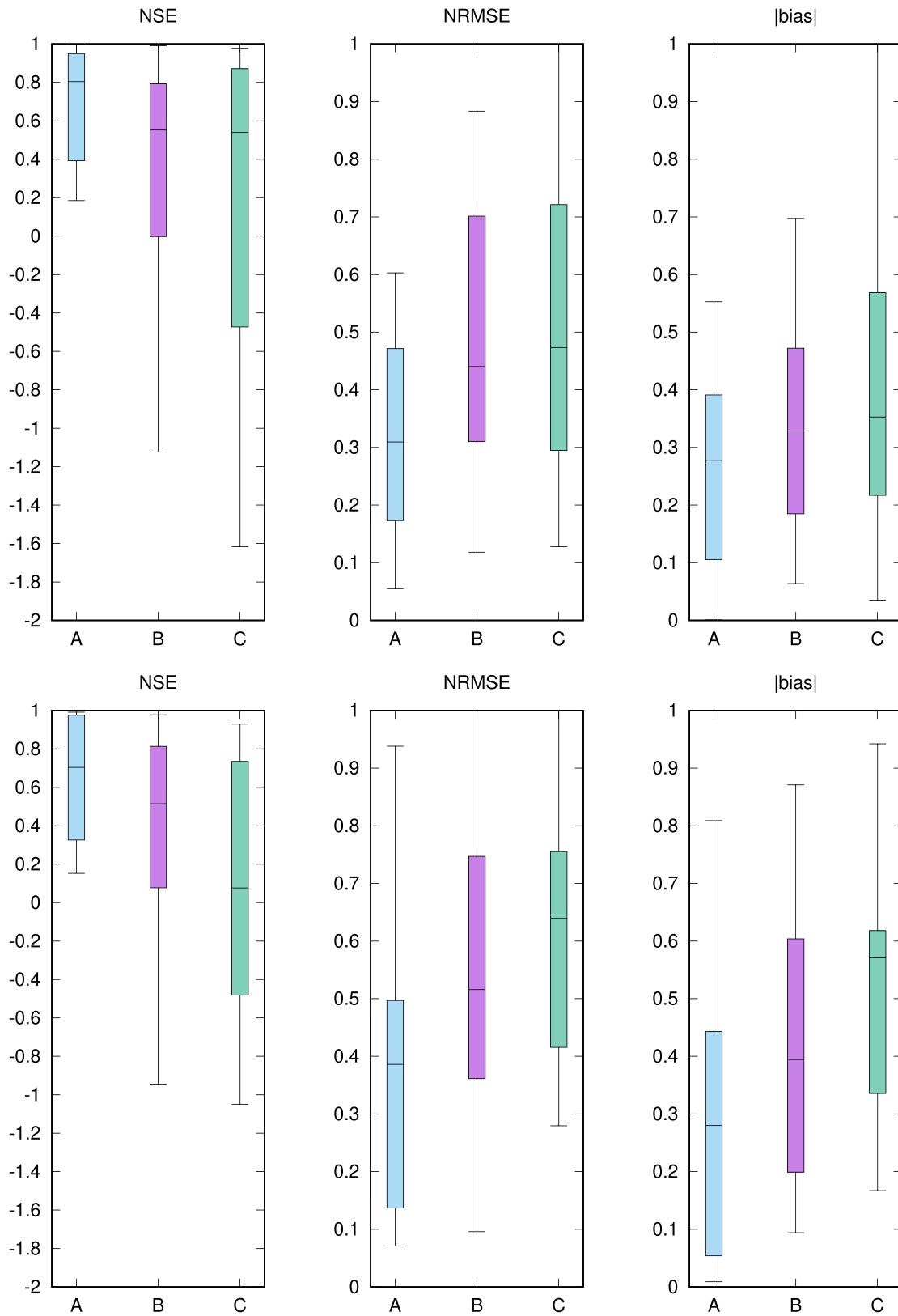


Fig. 11. Performance metrics by different methods involving the spatially averaged discharge: A – SIC-BVC, B – MetroMan, C – HiVDI. PEPSI-II ideal cases. Top subplots – 1 day snapshot period, bottom subplots – 4 days snapshot period.

Table 3
Comparative performance (NRMSE) by different methods, PEPsi-2.

	Case	SIC-BVC	MetroMan	HIVDI	GeoBAM	SADS
20	ArialKhan	0.471	0.319	1.281	3.869	0.693
21	AshSlough	0.186	0.364	0.173	0.408	0.401
22	BerendaSlough	0.364	0.741	1.035	1.987	1.335
23	Brahmaputra	0.527	0.746	0.337	2.038	1.154
24	ChowchillaCan	0.308	0.168	0.870	2.428	1.510
25	FresnoRiver	0.088	0.421	0.175	0.180	0.373
26	GrantLineCan	0.565	0.118	0.127	0.225	0.089
27	IowaRiver	0.174	0.824	0.432	1.031	2.366
28	Jamuna	0.140	0.592	0.633	0.093	—
29	Kushiyara	0.206	0.413	0.225	1.285	0.538
30	MariposaBypass	0.120	0.488	0.304	0.045	0.600
31	MercedRiver	0.190	0.192	0.239	0.310	0.275
32	MiddleRiver	8.151	5.484	4.102	4.059	1.257
33	Mississippi In	0.311	0.324	0.431	0.524	0.334
34	Missouri DS	0.298	0.302	0.599	0.476	0.347
35	Missouri MS	0.420	0.661	0.632	0.532	0.664
36	Missouri US	0.450	0.325	0.663	0.514	0.570
37	Ohio Section 1	0.477	0.459	0.193	0.662	0.401
38	Ohio Section 2	0.055	0.261	0.286	0.323	0.700
39	Ohio Section 3	0.151	0.278	0.402	0.128	0.457
40	Ohio Section 4	0.072	0.383	0.626	1.057	0.747
41	Ohio Section 5	0.251	0.524	0.599	0.219	0.465
42	Ohio Section 7	0.603	0.573	0.708	0.490	0.302
43	Ohio Section 8	0.436	0.791	0.734	0.646	0.871
44	Olentangy	7.603	7.478	8.199	9.206	8.166
45	Padma	0.472	0.883	1.216	1.032	1.183
46	SanJoaquin	0.172	0.149	0.388	0.414	0.702
47	SanJoaquin 2	1.425	1.444	4.906	4.360	0.536
48	Seine DS	0.181	0.462	0.209	0.247	0.842
49	Seine US	0.372	0.333	0.305	0.216	0.283
50	Stanislaus Riv	0.123	0.230	0.515	0.805	1.082
51	Tuolumne Riv	0.346	0.511	0.351	0.261	0.228

expert assessment of the L-curve.

In terms of accuracy, the SIC-BVC algorithm shows a superior performance (measured in NSE, NRMSE and NBIAS) in comparison to all SWOT DAWG algorithms reported in Frasson et al. (2021). For example, on the PEPsi-2 testing set, it gives about 25–30% improvement over the MetroMan, which itself shows the best performance among other SWOT DAWG algorithms. Moreover, our results on the complete PEPsi-1/2 testing set are better than those obtained on the PEPsi-2 set alone.

In terms of accuracy, the SIC-BVC algorithm shows a superior performance (measured in NSE, NRMSE and NBIAS) in comparison to all SWOT DAWG algorithms reported in Frasson et al. (2021). For example, on the PEPsi-2 testing set, it gives about 25–30% improvement over the MetroMan, which itself shows the best performance among other SWOT DAWG algorithms. Moreover, our results on the complete PEPsi-1/2 testing set are better than those obtained on the PEPsi-2 set alone. The above comparison is made with a few reservations, presented in the last paragraph of Section 6). We also admit a possibility that the mentioned SWOT DAWG algorithms could have been evolved, since the results reported in Frasson et al. (2021) were actually obtained. Intuitively, the accuracy of our method is approaching the limit, given the available data. This accuracy is clearly worse than the one that could be achieved using gauge measurements, however it may suffice for certain scientific and practical purposes.

This study has been focused on the proof of the concept of the new method, thus the issue of computational feasibility has not got much attention. We assess that the method in its present form can be used at a regional scale in a ‘hind cast’ or ‘reanalysis’ mode. For the global scale application in real or close-to-real time mode we suggest the generalized discharge estimator described in Section 4.8, which will use the ‘best currently available’ likelihood matrix. The computation of this matrix is a separate ‘learning’ process which may not necessarily be synchronized with data streams. There are also a few possible ways of reducing the computational cost of the likelihood matrix. One of them is to use the steady-state Saint–Venant solver instead of the transient solver (work in

progress). The importance of having the full complexity algorithm for the upcoming development of simplified versions is obvious: one can see what approximations could be accepted without a significant deterioration in the estimation accuracy.

Declaration of Competing Interest

The authors declare the following financial interests/personal relationships which may be considered as potential competing interests: Jérôme MONNIER, Professor in Applied Mathematics Computational Sciences, INSA (Institute Nationale des Sciences Appliquees), Toulouse, France.

Acknowledgments

I. Gejadze, P.-O. Malaterre and H. Oubanas have been co-funded by CNES Tosca research project, years 2014–2020. The joint work of V. Shutyaev and I. Gejadze was partially supported by the Russian Science Foundation (project 20–11-20057, in the part of research of Section 3). The work of V. Shutyaev is also co-funded by the Moscow Center for Fundamental and Applied Mathematics (agreement with the Ministry of Education and Science of the Russian Federation No.075–15-2019–1624). The authors thank T. Pavelsky for useful suggestions which helped to improve the paper, and R. Frasson for the data used for comparison of different discharge estimation algorithms.

References

- Alifanov, O.M., Artyukhin, E.A., Rummyantsev, S.V., 1996. *Extreme Methods for Solving Ill-Posed Problems with Applications to Inverse Heat Transfer Problems*. Begel House Publishers.
- Altenau, E.H., Pavelsky, T.M., Durand, M.T., Yang, X., Frasson, R.P. d. M., and Bendezu, L. (2021). The surface water and ocean topography (SWOT) mission river database (SWORD): A global river network for satellite data products. *Water Resour. Res.*, v. 57, e2021WR030054 doi: 10.1029/2021WR030054.

- Andreadis, K.M., Clark, E.A., Lettenmaier, D.P., Alsford, D.E., 2007. Prospects for river discharge and depth estimation through assimilation of swath-altimetry into a raster-based hydrodynamics model. *Geophys. Res. Lett.* 34, L10403. <https://doi.org/10.1029/2007gl029721>.
- Andreadis, K.M., Brinkerhoff, C.B., Gleason, C.J., 2020. Constraining the assimilation of SWOT observations with hydraulic geometry relations. *Water Resour. Res.* 56 <https://doi.org/10.1029/2019WR026611> e2019WR026611.
- Barnes, Harry H. Jr., 1967. *Roughness Characteristics of Natural Channels*. Geological Survey Water-Supply Paper 1849. United States Government Printing Offices, Washington.
- Baume, J.-P., Malaterre, P.-O., Belaud, G., Le Guenec, B. (2005). SIC: a 1D Hydrodynamic Model for River and Irrigation Canal Modeling and Regulation, Métodos Numéricos em Recursos Hídricos 7, ABRH (Associação Brasileira de Recursos Hídricos), Coppetec Fundacao, Editor Rui Carlos Vieira da Silva, pp. 1–81.
- Beal, M.J., 2003. *Variational Algorithms for Approximate Bayesian Inference*. University of London, London.
- Beal, M., Ghamarani, Z., 2003. The variational Bayesian EM algorithm for incomplete data: with application to scoring graphical model structures. In: Bernardo, J.M., Bayarri, M.J., Berger, J.O., Dawid, A.P., Heckerman, D., Smith, A.F.M., West, M. (Eds.), *Bayesian Statistics 7*. Oxford University Press, Oxford, pp. 1–10.
- Biancamaria, S., Durand, M., Andreadis, K.M., et al., 2011. Assimilation of virtual wide swath altimetry to improve Arctic river modeling. *Remote Sens. Environ.* 115 (2), 373–381. <https://doi.org/10.1016/j.rse.2010.09.008>.
- Biancamaria, S., Dennis P. Lettenmaier, D.P., Pavelsky, T.M. (2016). The SWOT mission and its capabilities for land hydrology. *Surv. Geophys.*, v. 37, n. 2, pp. 307–337.
- Blei, D.M., Kucukelbir, A., McAuliffe, J.D., 2017. Variational Inference: A Review for Statisticians. *J. Am. Stat. Assoc.* 112 (518), 859–877. <https://doi.org/10.1080/01621459.2017.1285773>.
- Brent, R.P., 1973. *Algorithms for Minimization without Derivatives*. Prentice-Hall, Englewood Cliffs, New Jersey, p. 195.
- Byrd, R.H., Lu, P., Nocedal, J., Zhu, C.A., 1995. Limited Memory Algorithm for Bound Constrained Optimization. *SIAM J. Sci. Comput.* 16 (5), 1190–1208. <https://doi.org/10.1137/0916069>.
- Cunge, J.A., Holly, F.M., Verwey, A. *Practical Aspects of Computational River Hydraulics*. Boston: Pitman Advanced Pub. Program, 1980. Print.
- Domeneghetti, A., Schumann, G.J.-P., Frasson, R.P.M., Wei, R., Pavelsky, T.M., Castellarin, A., et al., 2018. Characterizing water surface elevation under different flow conditions for the upcoming SWOT mission. *J. Hydrol.* 561, 848–861. <https://doi.org/10.1016/j.jhydrol.2018.04.046>.
- Domeneghetti, A., Molari, G., Tourian, M.J., Tarpanelli, A., Behnia, S., Moramarco, T., Sneeuw, N., Bratha, A., 2021. Testing the use of single-and multi-mission satellite altimetry for the calibration of hydraulic models. *Adv. Water Resour.* 151, 103887 <https://doi.org/10.1016/j.advwatres.2021.103887>.
- Durand, Michael, et al., 2010. The surface water and ocean topography mission: Observing terrestrial surface water and oceanic submesoscale eddies. *Proc. IEEE* 98 (5), 766–779.
- Durand, M., Neal, J., Rodriguez, E., Andreadis, K.M., Smith, L.C., Yoon, Y., 2014. Estimating reach-averaged discharge for the River Severn from measurements of river water surface elevation and slope. *J. Hydrol.* 511, 92–104. <https://doi.org/10.1016/j.jhydrol.2013.12.050>.
- Durand, M., Gleason, C.J., Garambois, P.A., Bjerklie, D., Smith, L.C., Roux, H., et al., 2016. An intercomparison of remote sensing river discharge estimation algorithms from measurements of river height, width, and slope. *Water Resour. Res.* 52, 4527–4549. <https://doi.org/10.1002/2015wr018434>.
- Durand, M.T., Chen, C., Frasson, R.P.D.M., Pavelsky, T., Williams, B., Yang, X., Fore, A., 2020. How will radar layover impact SWOT measurements of water surface elevation and slope, and estimates of river discharge? *Remote Sens. Environ.* 247, 111883 <https://doi.org/10.1109/igarss39084.2020.9323156>.
- Dyer, K.R., 1973. *Estuaries: a Physical Introduction*. John Wiley, New York, p. 140.
- Evensen, G., 1994. Sequential data assimilation with a nonlinear quasi-geostrophic model using Monte-Carlo methods to forecast error statistics. *J. Geophys. Res.* 99 (C5), 10143–10162. <https://doi.org/10.1029/94JC00572>.
- Frasson, R.P.D.M., Wei, R., Durand, M., Minear, J.T., Domeneghetti, A., Schumann, G., et al., 2017. Automated river reach definition strategies: Applications for the Surface Water and Ocean Topography Mission. *Water Resour. Res.* 53 (10), 8164–8186. <https://doi.org/10.1002/2017wr020887>.
- Frasson, R.P.M., Durand, M.T., Larnier, K., Gleason, C., Andreadis, K.M., Hagemann, M., et al., 2021. Exploring the factors controlling the error characteristics of the Surface Water and Ocean Topography mission discharge estimates. *Water Resour. Res.* 57 <https://doi.org/10.1029/2020wr028519> e2020WR028519.
- Garambois, P.A., Monnier, J., 2015. Inference of effective river properties from remotely sensed observations of water surface. *Adv. Water Resour.* 79, 103–120. <https://doi.org/10.1016/j.advwatres.2015.02.007>.
- Gejadze, I., Malaterre, P.-O., 2017. Discharge estimation under uncertainty using variational methods with application to the full Saint-Venant hydraulic network model. *Int. J. Numer. Meth. Fluids* 83 (5), 405–430. <https://doi.org/10.1002/fld.4273>.
- Gleason, C.J., Durand, M.T., 2020. Remote sensing of river discharge: A review and a framing for the discipline. *Remote Sensing* 12 (7), 1107. <https://doi.org/10.3390/rs12071107>.
- Gleason, C.J., Smith, L.C., Lee, J., 2014. Retrieval of river discharge solely from satellite imagery and atmanystations hydraulic geometry: Sensitivity to river form and optimization parameters. *Water Resour. Res.* 50, 9604–9619. <https://doi.org/10.1002/2014WR016109>.
- Hansen, P.C., O’Leary, D.P., 1993. The use of the L-curve in the regularization of discrete ill-posed problems. *SIAM J. Sci. Comput.* 14 (6), 1487–1503. <https://doi.org/10.1137/0914086>.
- Hagemann, M., Gleason, C.J., 2017. *Extracting Prior Distributions from a Large Dataset of In-Situ Measurements to Support SWOT-based Estimation of River Discharge*. In: AGU Fall Meeting Abstracts.
- Kaltenbacher B., Neubauer A., Scherzer O. (2008). Iterative Regularization Methods for Nonlinear Ill-posed Problems. Radon Series on Computational and Applied Mathematics. de Gruyter.
- Larnier, K., Monnier, J., Garambois, P.-A., Verley, J., 2020. River discharge and bathymetry estimation from SWOT altimetry measurements. Inverse problems in science and engineering 29 (6), 759–789. <https://doi.org/10.1080/17415977.2020.1803858>.
- Leopold, L.B., Maddock, T., 1953. *The Hydraulic Geometry of Stream Channels and Some Physiographic Implications*. USGS Professional Paper No 252, 1–57.
- Lin, P., Pan, M., Beck, H.E., Yang, Y., Yamazaki, D., Frasson, R., et al., 2019. Global reconstruction of naturalized river flows at 2.94 million reaches. *Water Resour. Res.* 55, 6499–6516. <https://doi.org/10.1029/2019WR025287>.
- Malaterre, P.-O., Dorchie, D., Baume, J.-P. (2014). Simulation and Integration of Control for Canals software (SIC²), for the design and verification of manual or automatic controllers for irrigation canals. USCID Conference on Planning, Operation and Automation of Irrigation Delivery Systems, Phoenix, Arizona.
- Marcus, W.A., Fonstad, M.A., 2010. Remote sensing of rivers: the emergence of a subsdiscipline in the river sciences. *Earth Surf. Proc. Land.* 35, 1867–1872. <https://doi.org/10.1002/esp.2094>.
- McCabe, M.F., et al., 2017. The future of Earth observation in hydrology. *Hydrology and earth system sciences* 21, 3879–3914. <https://doi.org/10.5194/hess-21-3879-2017>.
- McLachlan, G., Krishnan, T., 2007. *The EM Algorithm and Extensions*, vol 382. John Wiley & Sons, Hoboken, NJ.
- Merrel, M.K., Smith, L.C., Andreadis, K.M., Durand, M.T., 2013. Estimation of river depth from remotely sensed hydraulic relationships. *Water Resour. Res.* 49, 3165–3179 <https://doi.org/10.1002/wrcr.20176>.
- Neal, J., Hawker, L., Savage, J., Durand, M., Bates, P., Sampson, C., 2021. Estimating river channel bathymetry in large scale flood inundation models. *Water Resour. Res.* 57 <https://doi.org/10.1029/2020WR028301> e2020WR028301.
- Nicollet, G., Uan, M., 1979. *Ecoulements permanents surface libre en lits compos.* La Houille Blanche 1, 21–30.
- Oki, T., Kanae, S., 2006. Global hydrological cycles and world water resources. *Science* 313 (5790), 1068–1072. <https://doi.org/10.1126/science.1128845>.
- Oubanas, H., Gejadze, I., Malaterre, P.-O., Mercier, F., 2018. River discharge estimation from synthetic SWOT-type observations using variational data assimilation and the full Saint-Venant hydraulic model. *J. Hydrol.* 559, 638–647. <https://doi.org/10.1016/j.jhydrol.2018.02.004>.
- Oubanas, H., Gejadze, I., Malaterre, P.O., Durand, M., Wei, R., Frasson, R.P.M., Domeneghetti, A., 2018. Discharge estimation in ungauged basins through variational data assimilation: The potential of the SWOT mission. *Water Resour. Res.* 54, 2405–2423. <https://doi.org/10.1002/2017WR021735>.
- Oubanas, H., Gejadze, I., Malaterre, P.-O., 2020. *River Discharge and Bathymetry in Ungauged Rivers using Multi-Sources Variational Data Assimilation*. In: AGU Fall Meeting Abstracts.
- Pujol, L., Garambois, P.-A., Finaud-Guyot, P., Monnier, J., Larnier, K., Mos, R., Biancamaria, S., Yesou, H., Moreira, D., Paris, A., Calmant, S., 2020. Estimation of multiple inflows and effective channel by assimilation of multi-satellite hydraulic signatures: The ungauged anabranching Negro river. *J. Hydrol.* 591, 125331 <https://doi.org/10.1016/j.jhydrol.2020.125331>.
- Revel, M., Ikeshima, D., Yamazaki, D., Kanae, S. (2021). A framework for estimating global-scale river discharge by assimilating satellite altimetry. *Water Resources Research*, submitted.
- Rodriguez, E., Renato Frasson, et al., 2021. SWOT Discharge Estimation for Multichannel Rivers. Presentation at the SWOT Science Team meeting. Science Group.
- Schaperow, J.R., Li, D., Margulis, S.A., Lettenmaier, D.P., 2019. A curve-fitting method for estimating bathymetry from water surface height and width. *Water Resour. Res.* 55, 4288–4303. <https://doi.org/10.1029/2019WR024938>.
- Tikhonov, A.N., Arsenin, V.Y., 1977. *Solutions of ill-posed problems*. Winston-Wiley, New-York.
- Tourian, M.J., C. Schwatke, C., Sneeuw, N. (2017). River discharge estimation at daily resolution from satellite altimetry over an entire river basin. *J. Hydrol.*, v. 546, pp. 230–247. doi: 10.1016/j.jhydrol.2017.01.009.
- Wisser, D., Fekete, B.M., Vorosmarty, C.J., Schumann, A.H., 2010. Reconstructing 20th century global hydrography: A contribution to the Global Terrestrial NetworkHydrology (GTNH). *Hydrol. Earth Syst. Sci.* 14 (1), 1–24. <https://doi.org/10.5194/hess1412010>.
- Yuan Yang, Y., Pan, M., Lin, P., Beck, H.E., Zeng Z., Yamazaki, D., David, C.H., Lu, H., Yang, K., Hong, Y., Wood, E.F., 2021. Global Reach-level 3-hourly River Flood Reanalysis (1980–2019). *Bull. Am. Meteorol. Soc.* In press. doi: 10.1175/BAMS-D-20-0057.1.